water

MDPI

Article

Research on Construction Control Measures for Enclosed Karst Tunnels

Miaoxin Zhang [1,2], Wei Meng [1,2,*], Xiaowei Zhang [3], Guotao Tang [1], Caiyang Sun [1], Xuefu Zhang [1,2], Jun Liu [4] and Xinzhen Li [3]

[1] School of Civil Engineering, Chongqing Jiaotong University, Chongqing 400074, China; zhangmiaoxin2025@163.com (M.Z.); tangguotao1126@163.com (G.T.); suncaiyang1123@163.com (C.S.); zhangxuefu20240821@163.com (X.Z.)
[2] Institute of Future Civil Engineering Sciences and Technology, Chongqing Jiaotong University, Chongqing 400074, China
[3] China Railway Changjiang Transport Design Group Co., Ltd., Chongqing 401121, China; zhangxiaowei204@163.com (X.Z.); lixinzhen457@163.com (X.L.)
[4] Chongqing High Speed Railway Construction Wankaida Expressway Co., Ltd., Chongqing 404100, China; liujun439@163.com
* Correspondence: mw@cqjtu.edu.cn

Abstract: This study explores the water inrush phenomenon and its control measures during tunnel construction in enclosed karst geological conditions through a real case study. Using numerical simulation methods, the study investigates the variations in water level drawdown, drainage volume, and the changes in principal stress and displacement at four locations (arch waist, left arch waist, left arch foot, and arch bottom) during tunnel construction under three excavation methods (full-face excavation method (FFEM,), bench excavation method (BEM), and reserved core soil excavation method (RCSEM)), six water head heights (122 m, 162 m, 202 m, 242 m, 282 m, 322 m), and five excavation advances (0.5 m, 1.0 m, 1.5 m, 2.0 m, 2.5 m). The results show that, compared to controlling excavation advance, water level drawdown and drainage volume are more sensitive to increases in initial water head height. The reserved core soil method results in the smallest drainage volume and water level drawdown, effectively controlling stress increase and significantly mitigating arch bottom uplift. The RCSEM has the smallest drainage volume, making it an ideal choice for ecological protection.

Keywords: enclosed karst geological structure; tunnel excavation; numerical simulation; fluid–structure interaction

Received: 10 January 2025
Revised: 27 January 2025
Accepted: 29 January 2025
Published: 31 January 2025

Citation: Zhang, M.; Meng, W.; Zhang, X.; Tang, G.; Sun, C.; Zhang, X.; Liu, J.; Li, X. Research on Construction Control Measures for Enclosed Karst Tunnels. *Water* **2025**, *17*, 389. https://doi.org/10.3390/w17030389

1. Introduction

In the mountainous regions of Southwest China, there exists a unique geological structure known as the enclosed karst geological structure. This structure is characterized by highly permeable rock layers rich in groundwater that are tightly encased by less permeable rock layers, forming a special hydrogeological unit with strong water storage capacity and significantly elevated water pressure. When tunnel construction passes through the boundary zones of such formations, the disturbance to the mountain's equilibrium caused by excavation may lead to sudden and high-intensity water inrush. This poses risks to construction safety, project progress, and the long-term stability of the tunnel structure. At the same time, the system balance between groundwater and the ecological environment around the tunnel construction area is disrupted, potentially resulting

in incidents such as groundwater level decline, reduced effective stress of the surrounding rock, ground subsidence, and surface vegetation wilting [1–14]. These issues can lead to difficulties in accessing water, environmental degradation in the surrounding construction area, and significant safety risks to the lives and properties of nearby residents.

The seepage field refers to the dynamic hydrological phenomenon of groundwater flow within the pores and fracture networks of rock and soil masses. It has a significant impact on the physical properties, mechanical behavior, and safety of engineering construction in these materials. To investigate the disturbances to the seepage field caused by tunnel excavation, some researchers have employed finite element software to conduct refined numerical simulations of the tunnel construction process [15–22]. These studies explored the distribution characteristics and dynamic changes of the seepage and stress fields in the surrounding rock before and after excavation, providing a theoretical basis for understanding and predicting seepage responses during excavation. On this foundation, new approaches to addressing tunnel seepage issues have been proposed. Many researchers, starting from theoretical perspectives, have optimized key parameters in seepage models for rock and soil masses. A novel alternate analytical method was introduced to obtain an exact solution for the steady-state seepage field around underwater twin tunnels in a semi-infinite saturated aquifer, accurately accounting for the influence of lining or grouting zones and the interaction of tunnel seepage [23]. An analytical solution for the seepage field in water-rich rock layers composed of surrounding rock, grouting rings, and primary support was derived [24]. Additionally, analytical solutions for the impact of tunnel construction on seepage fields have been developed, enabling further prediction of tunnel water inflow rates [25–32].

Although the issue of water inflow in tunnels has garnered significant attention, research on steady seepage and water inflow in water-rich karst tunnels is still in its early stages and requires further exploration. This study focuses on the Wufu Tunnel in Chongqing, establishing a three-dimensional fluid–structure interaction model of the tunnel excavation process. The research systematically investigates the impact of tunnel construction on the stability of the surrounding rock and the groundwater environment. This not only enriches the theoretical understanding of the design and construction of enclosed karst tunnels but also provides practical reference guidelines for the planning and implementation of similar engineering projects.

2. Project Overview

The Wanzhou to Kaizhou Expressway is a section of the G5012 National Highway Network's transverse connection line. It is located in the northeastern Chongqing region, connecting Wanzhou and Kaizhou districts. The route begins at Lushan in Wanzhou, connecting to the G5012 (Wanzhou South Ring) Expressway, passing through Lihe Town, crossing Tiefeng Mountain, continuing through Nanmen Town and Jiacao Mountain, then through Tieqiao Town, and finally reaching the Nanya Interchange near Nanya, where it connects to the Kaikai Road to enable traffic transitions. The total route length is 47.481 km. The entrance to the Wufu Tunnel is located in Shengji Village, Nanmen Town, Kaizhou District, and its exit is in Yuhe Village, Tieqiao Town. The tunnel features a twin-tube design with a distance of 15–30 m between the left and right lanes. The tunnel has a slightly arched alignment extending to the southwest, with an overall direction of approximately 328°. The tunnel is designed for a speed of 100 km/h, with a structural clearance width of 10.75 m. The radius of the tunnel arch waist is 5.80 m, and the cross-sectional area is 67.08 m^2.

Taking the left tunnel as an example, geological survey data indicate that the interface between the impermeable rock layer T2b2 and the permeable rock layer T2b1 is located at tunnel position ZK38 (see Figure 1). The surrounding rock is classified as Grade

V. The tunnel prototype at this location adopts the S5c-type lining cross-section (see Figure 2). The initial support for the tunnel uses C25 concrete with a thickness of 0.24 m, while the secondary lining uses C35 concrete with a thickness of 0.45 m. The construction methods considered include the full-face excavation method (abbreviated hereinafter: FFEM), the bench excavation method (abbreviated hereinafter: BEM), and the reserved core soil excavation method (abbreviated hereinafter: RCSEM).

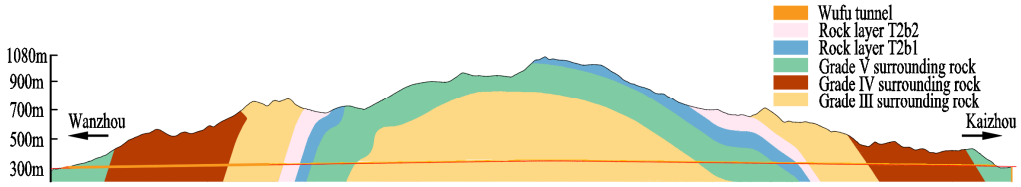

Figure 1. Geological profile of the left tunnel.

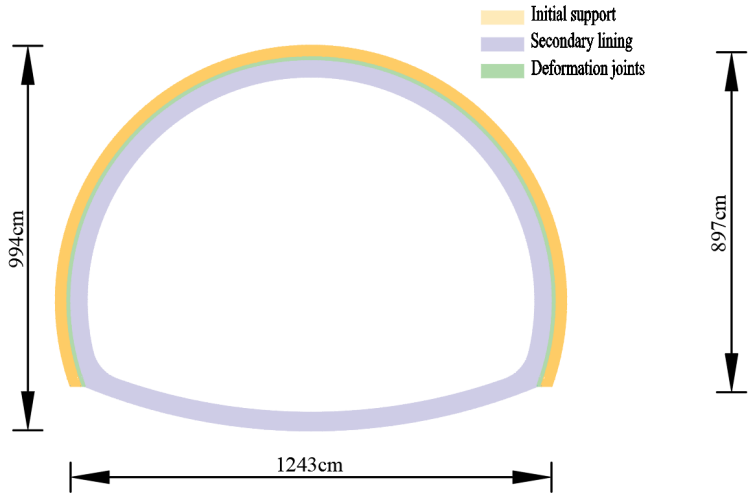

Figure 2. S5c-type lining cross-section.

The seepage model assumes isotropy, and the relevant material parameters for the model are shown in Table 1 (where "—" stands for infinity).

Table 1. Model material parameters.

Materials	Density P (kg·m^{-3})	Elastic Modulus E (GPa)	Poisson's Ratio μ	Cohesion C (MPa)	Internal Friction Angle φ (°)	Permeability Coefficient K (m/d)	Porosity
Low-permeability rock layer: T2b2	2550	8.2	0.34	5.87	32.35	0.03	0.35
Highly permeable rock layer: T2b1	2500	6.2	0.33	3.08	39.30	0.42	0.35
Initial support	2700	28.0	0.21	—	53.85	8.64×10^{-6}	0.21
Secondary lining	3000	30.0	0.19	—	55.91	8.64×10^{-7}	0.19

3. Establishment of the Three-Dimensional Fluid–Structure Interaction Model for Tunnel Excavation Process and Seepage Field Analysis

This section may be divided by subheadings. It should provide a concise and precise description of the experimental results, their interpretation, as well as the experimental conclusions that can be drawn.

3.1. Establishment of the Three-Dimensional Fluid–Structure Interaction Model for Tunnel Excavation Process

Numerical simulations were conducted using ABAQUS 2022 software. In this study, to highlight the characteristics of the enclosed karst geological structure and simplify the model, the interface between the weakly permeable rock layer T2b2 and the highly permeable rock layer T2b1 was chosen as the research object (Figure 3). A three-dimensional fluid–structure interaction model for the tunnel excavation process was established. The study analyzed the impact and variation of the stress field, displacement field, and pore water pressure field during the excavation process under different working conditions and construction methods, and explored reasonable construction plans.

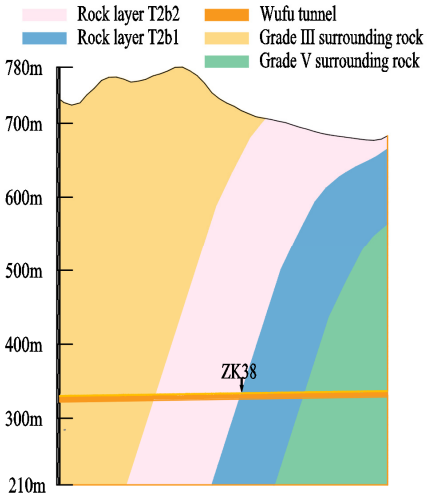

Figure 3. Location of the interface between T2b2 and T2b1.

To minimize the boundary effect, a distance of 100 m is taken on each side, corresponding to the model depth. The geological layers are symmetrically distributed in the front and rear. The red-brown color represents the weakly permeable rock layer T2b2, and the light blue color represents the highly permeable rock layer T2b1. According to geological survey data, the underground river recharge at this location is 373 m away from the tunnel in a straight line, which corresponds to the distance from the centerline of the tunnel to the ends of the model. The tunnel depth is 322 m, which corresponds to the distance from the tunnel arch waist to the top of the model. The model height is set to 500 m. The model dimensions are 746 m × 500 m × 200 m. The front, rear, left, and right boundaries of the model are constrained for normal displacement, with a free boundary at the top and a fixed boundary at the bottom.

The seepage model uses an isotropic seepage model, with the bottom and the front, rear, and side boundaries set as impermeable. The recharge is set as fixed water head recharge on both sides, and rainfall is applied at the surface with a rainfall intensity of 1266.6 mm, which is the average annual rainfall intensity for the tunnel site. The initial water level, or fixed water head recharge, is simulated with different gradient groups according to the actual conditions. To simulate the groundwater discharge during the tunnel construction process, the tunnel's inner surface is set as a discharge boundary with a pore water pressure of 0 MPa, representing a free discharge boundary. The model has a total of 142,933 nodes and 135,936 elements, using linear hexahedral elements with element type C3D8P. Figure 4 is a schematic diagram of the model, where (a) is a schematic diagram of the model grid; (b) is a schematic diagram of the FFEM; (c) is a schematic diagram of the BEM; (d) is a schematic diagram of the RCSEM. Considering the practical engineering conditions, when using the BEM and the RCSEM for step-by-step excavation, a certain

construction step distance needs to be reserved. During one construction cycle, different excavation footages are used to excavate the upper step (BEM)/arch-shaped guiding tunnel and the left and right sidewall guiding tunnels sequentially (RCSEM). The lower step (BEM)/reserved core soil is then excavated in the same manner (RCSEM).

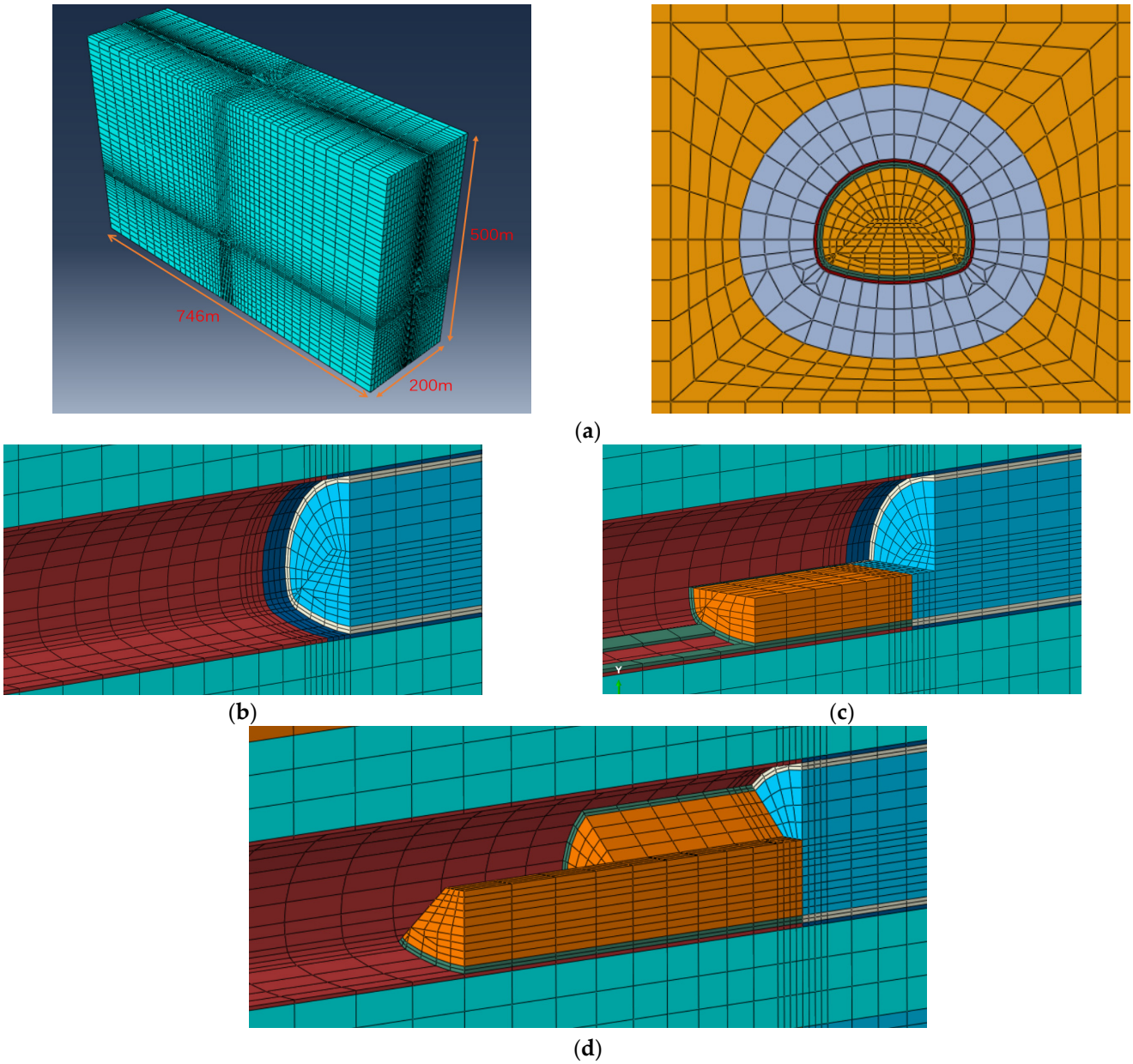

Figure 4. Schematic of the model(In the figure, (**a**):Schematic of the model mesh; (**b**): Schematic of FFEM ; (**c**): Schematic of BEM excavation; (**d**): Schematic of RCSEM ;cyan represents the surrounding rock strata, sky blue represents the soil in the tunnel excavation direction, orange in c/d represents the rock mass excavated step by step, and red represents the tunnel that has been excavated.).

A monitoring section is set at the interface between the highly permeable and weakly permeable rock layers at Z = 100 m in the middle of the model. Figure 5 shows the arrangement of the surrounding rock monitoring points. Since the model is symmetric, monitoring points are only set in the left half of the tunnel, located at the arch waist, left arched waist, left arched foot, and arched bottom. The positions of the monitoring points are shown in Figure 5.

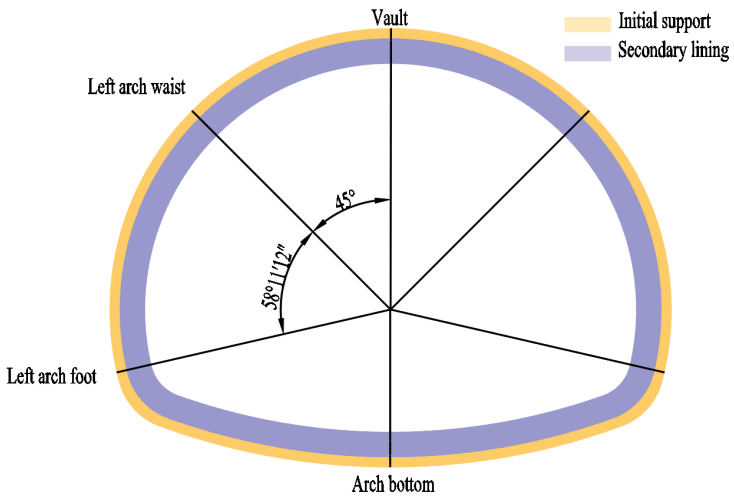

Figure 5. Tunnel monitoring point layout.

Displacement around the tunnel is a measurable indicator and is the most direct basis for assessing tunnel stability after excavation. In this study, the tunnel is buried deeper than 300 m and located in a water-rich V-grade surrounding rock area. According to the Highway Tunnel Design Code (JTG 3370.1—2018) [33], the allowable relative horizontal convergence vault around the tunnel is 1% to 3%, and the allowable settlement vault of the arch waist is 0.5 to 1 times 1% to 3%. Due to the highwater pressure and higher risk of water inrush in this section, both the allowable relative horizontal convergence vault and the allowable arch waist settlement vault are set to the lower limits. Therefore, the horizontal convergence limit vault is 129.8 mm, and the arch waist settlement limit vault is 64.9 mm.

Based on the rock physical and mechanical test data from the survey report, the compressive strength of the weakly permeable rock layer in the segment from ZK37 + 900 to ZK38 and the highly permeable rock layer from ZK38 to ZK38 + 100 were reduced according to the Municipal Engineering Geological Survey Code (BJ50-174-2014) [34]. The compressive strength of the weakly permeable rock layer is 28.17 MPa, and the tensile strength is 1.5 MPa; the compressive strength of the highly permeable rock layer is 15.33 MPa, and the tensile strength is 1.4 MPa. To ensure tunnel safety, the smaller vault between the compressive and tensile strengths of the surrounding rock is taken. Therefore, the compressive strength is set to 15.33 MPa, and the tensile strength is set to 1.4 MPa. If the surrounding rock stress exceeds these vaults after tunnel excavation, it is considered a failure or instability.

3.2. Study on the Variation Law of Drainage Volume and Water Level Drawdown

Based on the characteristics of the geological formation and the actual project, three factors—water head height, excavation footage, and excavation method—were selected to discuss the impact of tunnel drainage on the pore water pressure field. The water head height is defined as HHH, with six different vaults: H = 122 m, H = 162 m, H = 202 m, H = 242 m, H = 282 m, and H = 322 m. The excavation footage is defined as L, with five different vaults: L = 0.5 m, L = 1.0 m, L = 1.5 m, L = 2.0 m, and L = 2.5 m. Three excavation methods were considered: FFEM, BEM, and RCSEM. A total of 90 working conditions were set, calculated as 6 × 5 × 3 = 90 groups.

The pore water pressure field cloud diagrams for each working condition under different excavation methods are shown in Figures 6–8. The initial water level drawdown and tunnel drainage volume data for each working condition under different excavation methods are extracted and shown in Table 2.

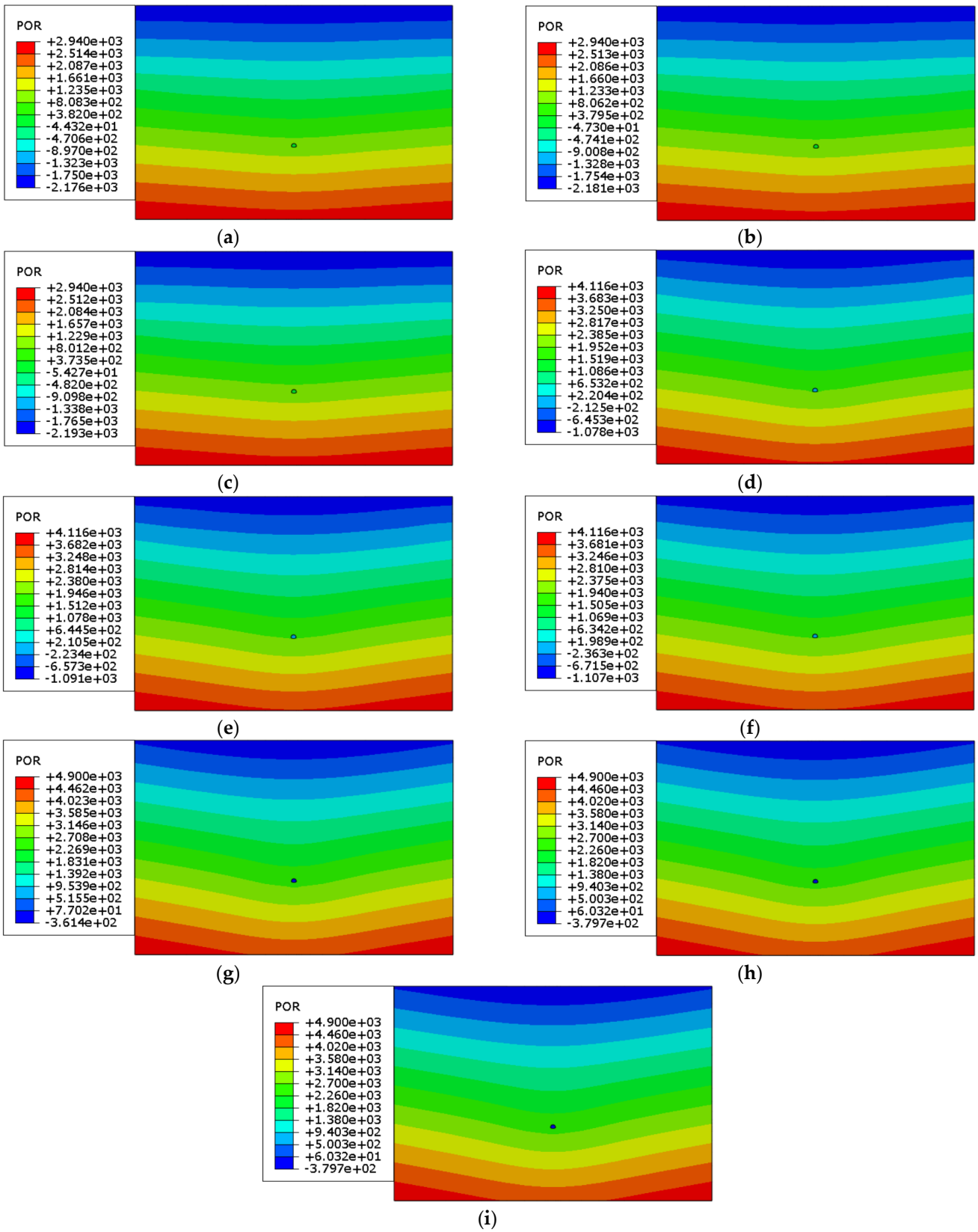

Figure 6. Pore water pressure field under different initial head heights (H) and different excavation footage (L) for FFEM. (In the figure, (**a**): H = 122 m and L = 0.5 m; (**b**): H = 122 m and L = 1.5 m; (**c**): H = 122 m and L = 2.5 m; (**d**): H = 242 m and L = 0.5 m; (**e**): H = 242 m and L = 1.5 m; (**f**): H = 242 m and L = 2.5 m; (**g**): H = 322 m and L = 0.5 m; (**h**): H = 322 m and L = 1.5 m; (**i**): H = 322 m and L = 2.5 m.).

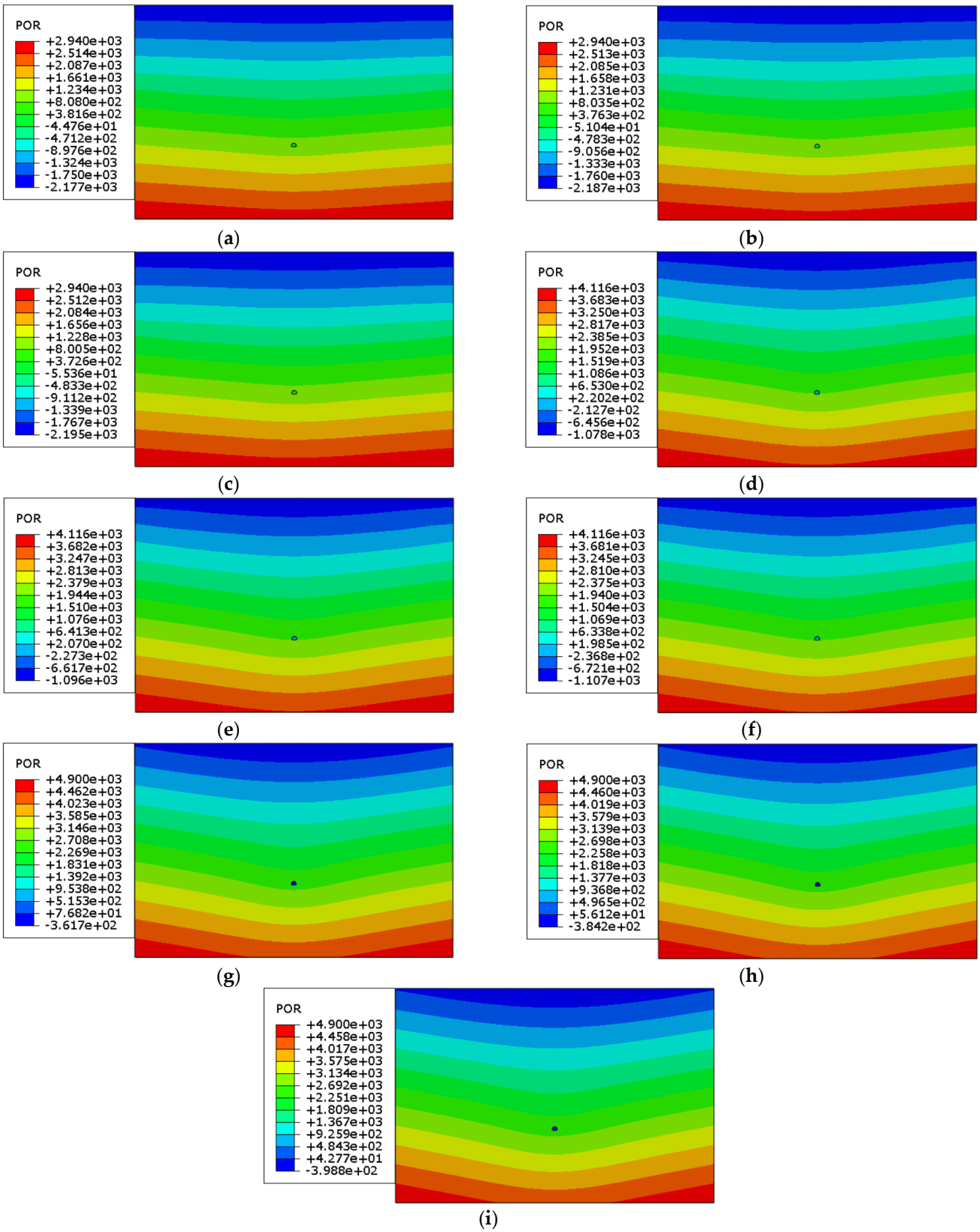

Figure 7. Pore water pressure field under different initial head heights (H) and different excavation footage (L) for BEM. (In the figure, (**a**): H = 122 m and L = 0.5 m; (**b**): H = 122 m and L = 1.5 m; (**c**): H = 122 m and L = 2.5 m; (**d**): H = 242 m and L = 0.5 m; (**e**): H = 242 m and L = 1.5 m; (**f**): H = 242 m and L = 2.5 m; (**g**): H = 322 m and L = 0.5 m; (**h**): H = 322 m and L = 1.5 m; (**i**): H = 322 m and L = 2.5 m.)

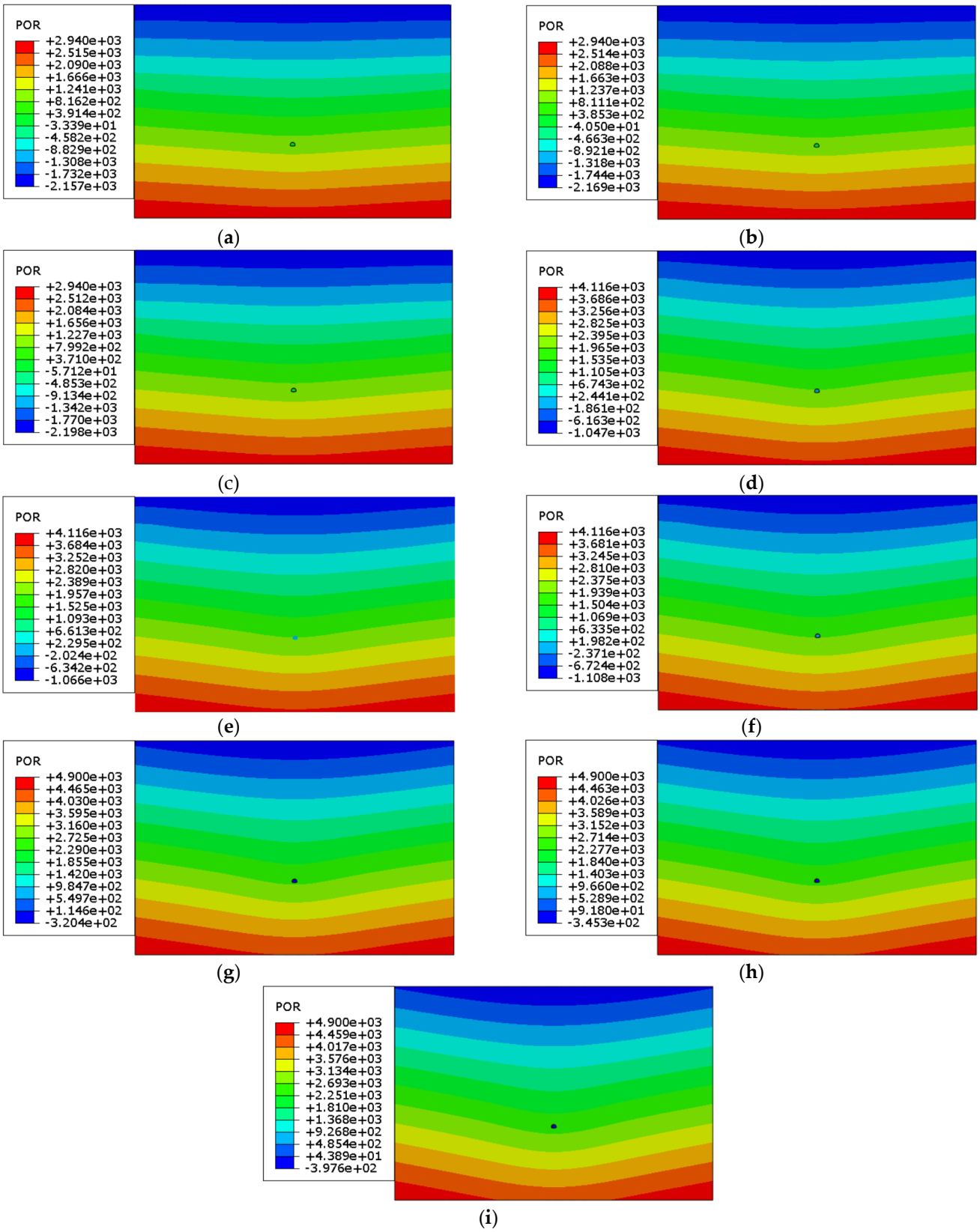

Figure 8. Pore water pressure field under different initial head heights (H) and different excavation footage (L) for RCSEM. (In the figure, (**a**): H = 122 m and L = 0.5 m; (**b**): H = 122 m and L = 1.5 m; (**c**): H = 122 m and L = 2.5 m; (**d**): H = 242 m and L = 0.5 m; (**e**): H = 242 m and L = 1.5 m; (**f**): H = 242 m and L = 2.5 m; (**g**): H = 322 m and L = 0.5 m; (**h**): H = 322 m and L = 1.5 m; (**i**): H = 322 m and L = 2.5 m.)

Table 2. Statistics of water level drawdown and drainage volume under different conditions and excavation methods.

Different Conditions		FFEM		BEM		RCSEM	
Excavation Footage (m)	Initial Water Head (m)	Drawdown of Water Level(m)	Drainage Volume $m^3/(m \cdot d)$	Drawdown of Water Level (m)	Drainage $m^3/(m \cdot d)$	Drawdown of Water Level (m)	Drainage Volume $m^3/(m \cdot d)$
0.5	122	25.84	13.40	25.70	13.35	22.37	11.63
0.5	162	27.94	18.07	27.93	18.01	24.92	15.42
0.5	202	29.60	21.86	29.48	21.80	25.88	19.21
0.5	242	31.23	26.53	31.13	26.45	27.49	22.99
0.5	282	33.48	30.86	33.44	30.77	29.32	26.75
0.5	322	36.79	35.15	36.65	35.05	32.46	30.47
1	122	26.64	14.76	26.62	14.72	23.50	12.18
1	162	28.78	18.73	28.62	18.69	25.66	16.15
1	202	30.58	22.71	30.46	22.66	27.14	20.12
1	242	32.27	28.06	32.23	28.00	28.65	24.09
1	282	34.46	32.00	34.44	31.93	30.74	28.02
1	322	37.91	35.90	37.88	35.83	33.66	31.92
1.5	122	27.51	14.82	27.19	14.79	24.26	13.07
1.5	162	29.40	19.16	29.12	19.13	26.55	16.63
1.5	202	31.21	23.26	31.09	23.23	28.06	20.74
1.5	242	33.26	28.14	32.91	28.09	29.45	24.83
1.5	282	35.18	32.73	35.07	32.68	31.65	28.89
1.5	322	38.89	37.28	38.47	37.23	34.88	32.90
2	122	27.98	15.75	27.93	15.65	25.65	14.43
2	162	30.22	20.10	30.14	19.98	26.94	19.16
2	202	32.78	24.20	32.69	24.09	29.53	23.90
2	242	33.85	31.09	33.83	30.78	30.93	28.63
2	282	36.10	34.61	36.04	34.23	33.12	32.70
2	322	39.68	39.16	39.63	38.78	36.51	37.96
2.5	122	28.50	16.39	28.46	16.08	28.44	14.60
2.5	162	30.76	20.59	30.75	20.30	30.72	19.39
2.5	202	32.69	25.39	32.66	25.10	32.65	24.19
2.5	242	34.77	31.97	34.45	31.12	34.35	28.98
2.5	282	36.68	37.20	36.67	36.21	36.62	33.71
2.5	322	39.76	42.37	39.70	41.24	39.68	38.40

3.2.1. Seepage Analysis at Different Water Head Heights

In tunnel engineering, the impact of water head height on drainage volume is a complex but crucial consideration. Its principle involves the basic theory of groundwater flow and the effect of tunnel construction on the surrounding geological environment. During the tunnel construction process, controlling the drainage volume not only concerns construction safety but also directly affects project quality and environmental protection. This study explores the variation law of drainage volume and water level drawdown under different initial water head heights, controlling the excavation footage at L=1.5 m, with initial water head heights set as H = 122 m, H = 162 m, H = 202 m, H = 242 m, H = 282 m, and H = 322 m. To visually describe the stress variation law at monitoring points, the ratio of the water level drawdown under different working conditions to the initial working condition water level drawdown is defined as the variation rate Δ', with the following formula:

$$\Delta' = \frac{s}{s_0} \times 100\% \quad (1)$$

where Δ' is the water level drawdown variation rate; s is the water level drawdown in meters; s_0 is the initial working condition water level drawdown in meters.

The ratio of the water level drawdown under different conditions to the initial working condition drainage volume is defined as the variation rate Δ, with the following formula:

$$\Delta' = \frac{q}{q_0} \times 100\% \quad (2)$$

where Δ' is drainage volume variation rate; q, drainage volume in $m^3/(m \cdot d)$; q_0, initial working condition drainage volume in $m^3/(m \cdot d)$.

In the analysis of different initial water head heights, H = 122 m is considered as the initial working condition. The water level drawdown, drainage volume variation curves, and variation rate curves are shown in Figures 9 and 10.

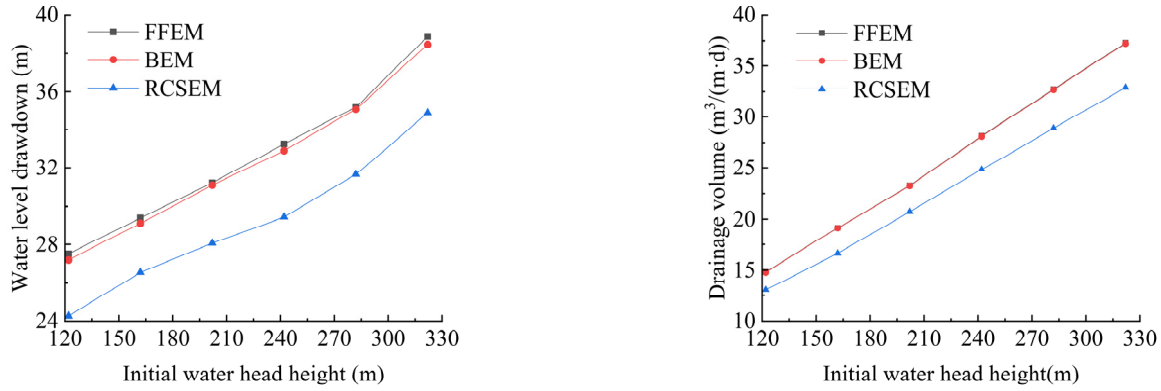

Figure 9. Water level drawdown/drainage volume variation curves at different initial water head heights.

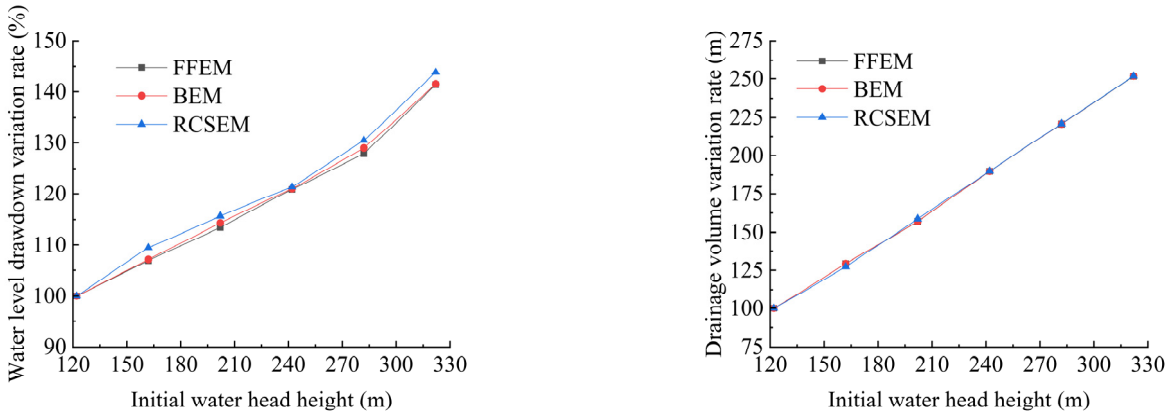

Figure 10. Water level drawdown/drainage volume variation rate curves at different initial water head heights.

(1) From the figure, it can be seen that as the initial water head height increases, both the water level drawdown and drainage volume increase under all three excavation methods. The drainage volume variation rate is higher than the water level drawdown variation rate for all three excavation methods, indicating that drainage volume is more sensitive to the increase in initial water head height than water level

drawdown. As the initial water head height increases, the change in drainage volume is more significant than the change in water level drawdown.

(2) Regarding different excavation methods, the increase in water level drawdown and drainage volume with rising initial water head height shows little variation among the three methods, indicating that the sensitivity of water level drawdown and drainage volume to increases in initial water head height is similar across the methods. In terms of the magnitude of drainage volume and water level drawdown, the order is FFEM > BEM > RCSEM (e.g., L = 1.5 m, H = 322 m, 37.28 > 37.23 > 32.90 (m^3/(m·d)); 38.89 > 38.47 > 34.88 (m)). Additionally, the numerical difference between the BEM and FFEM is small. Therefore, the RCSEM, with a smaller drainage volume and water level drawdown, is more suitable for water-rich karst tunnels where ecological protection must be considered.

3.2.2. Seepage Analysis at Different Excavation Distances

The variation law of drainage volume and water level drawdown under different excavation footage rates, with the initial head height controlled as the average water head height H = 282 m for the tunnel segment ZK37 + 900~ZK38 + 100, and excavation footages vaults of L = 0.5 m, L = 1.0 m, L = 1.5 m, L = 2.0 m, and L = 2.5 m.

In the analysis of different excavation footages, L = 0.5 m is taken as the initial condition. The curves of water level drawdown, drainage volume variation, and variation rate are shown in Figures 11 and 12.

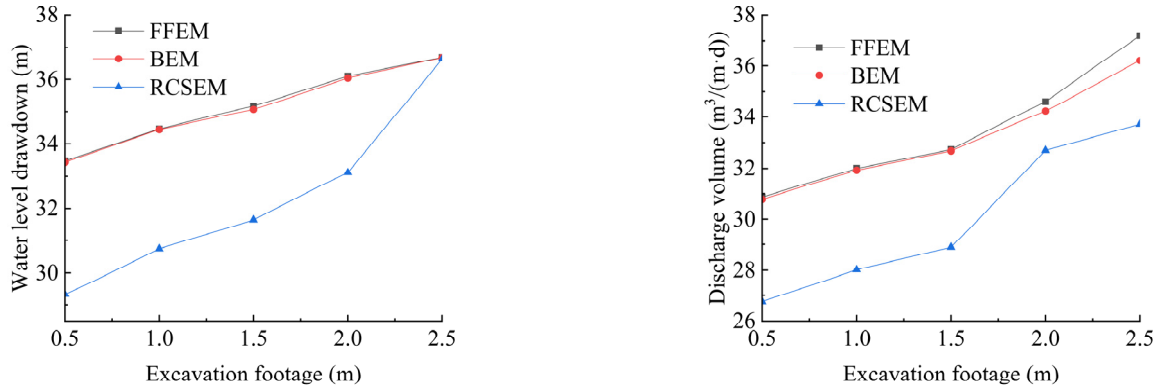

Figure 11. Water level drawdown/drainage volume variation curves under different excavation footages.

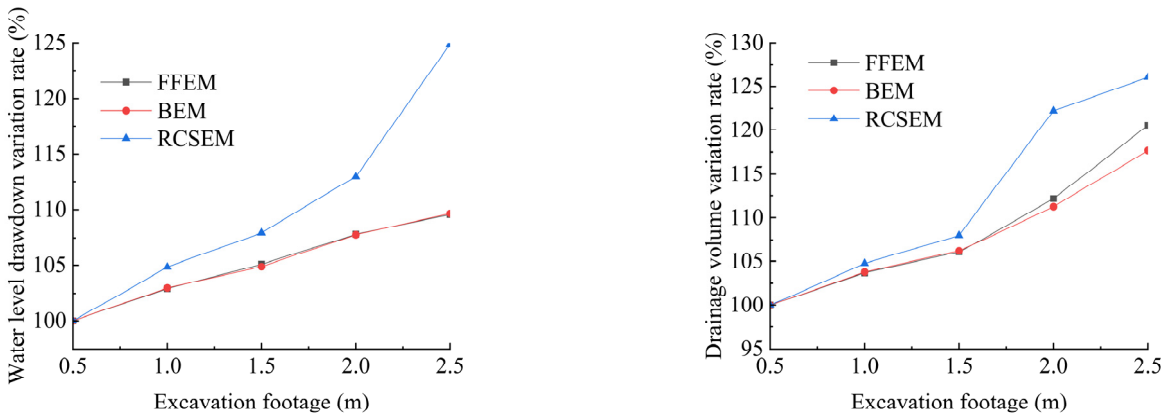

Figure 12. Water level drawdown/drainage volume variation rate curves under different excavation footages.

(1) As shown in the figure, with the increase in excavation footage, both water level drawdown and drainage volume increase under all three excavation methods. The drainage volume variation rate is greater than the water level drawdown variation rate for all three methods, indicating that drainage volume is more sensitive to the increase in excavation footage than water level drawdown.

(2) From the perspective of different excavation methods, the growth rates of water level drawdown and drainage volume with increasing excavation footage are similar across the three methods, suggesting that controlling excavation footage has a similar effect on all three excavation methods. Regarding the magnitude of drainage volume and water level drawdown, the sequence is as followsFFEM > BEM > RCSEM (e.g., L = 1.5 m, H = 282 m, 32.73 > 32.68 > 28.89 (m^3/(m·d)); 35.18 > 35.07 > 31.65 (m)). The numerical difference between the BEM and FFEM is small, indicating that controlling excavation footage to limit groundwater discharge and water level drawdown is more effective with the RCSEM.

(3) The geological environment changes caused by tunnel excavation directly affect the hydraulic properties of the surrounding strata. Specifically, tunnel excavation changes the spatial arrangement of geological media, reorganizing the groundwater flow paths and altering the distribution of the pore water pressure field. As a new spatial void, the tunnel disrupts the hydraulic equilibrium of the original strata, causing groundwater to converge into the tunnel space, forming new seepage paths. The excavation footage size directly affects the speed and direction of the redistribution of the pore water pressure field around the tunnel. Smaller excavation footage means slower construction, allowing more time for groundwater to adjust, which may result in smoother variations in seepage velocity and more uniform water head distribution. In contrast, a larger excavation footage will rapidly change the seepage conditions, potentially leading to a sudden increase in groundwater flow rate and enhancing the permeable flow in the surrounding strata.

3.2.3. Drainage Volume Variation Fitting Formula

The relationship between tunnel drainage volume and water level drawdown under different excavation methods and conditions is shown in Table 2. Through the above analysis, it is clear that the tunnel drainage volume is related to the initial water head height, excavation footage, and water level drawdown. Using water level drawdown as independent variable x_1, excavation footage as independent variable x_2, and initial water head height as independent variable x_3, the drainage volume is treated as the dependent variable y. Origin2018 software was used for the three-dimensional fitting analysis of the data.

The fitted drainage volume calculation formulas for different excavation methods are as follows: the formula for FFEM is Equation (3), for BEM is Equation (4), and for RCSEM is Equation (5).

$$y = 0.2054x_1 - 1.2939\left(\frac{x_1}{10}\right)^3 + 0.0508\left(\frac{x_1}{10}\right)^5 + 3.3164x_2 + 0.03761{x_2}^3 + 0.001568{x_2}^5 + 0.1879x_3 - 1.1536\left(\frac{x_3}{200}\right)^5 \quad (3)$$

$$y = 0.1458x_1 - 1.0089\left(\frac{x_1}{10}\right)^3 + 0.0402\left(\frac{x_1}{10}\right)^5 + 2.8132x_2 + 0.07252{x_2}^3 + 0.006155{x_2}^5 + 0.1711x_3 - 0.9537\left(\frac{x_3}{200}\right)^5 \quad (4)$$

$$y = -0.1201x_1 + 0.2267\left(\frac{x_1}{10}\right)^3 + 0.002046\left(\frac{x_1}{10}\right)^5 - 3.0347x_2 + 1.764{x_2}^3 - 0.2057{x_2}^5 + 0.1055x_3 - 1.5274\left(\frac{x_3}{200}\right)^5 \quad (5)$$

where y is drainage volume (m^3/(m·d)); x_1 is water level drawdown (m); x_2 is excavation footage (m); x_3 is initial water head height (m).

The goodness of fit for the FFEM, BEM, and RCSEM are $R^2 = 0.9364$, $R^2 = 0.9484$, and $R^2 = 0.9482$, respectively, indicating a good fitting result.

3.3. Stability Analysis of Surrounding Rock Under Different Initial Water Head Heights and Excavation Methods

3.3.1. Stress Field Analysis Under Different Initial Water Head Heights

This section analyzes the surrounding rock stress field under different water head heights. Figures 13–15 show the maximum and minimum principal stress contour maps of the surrounding rock at the monitoring section for different excavation methods.

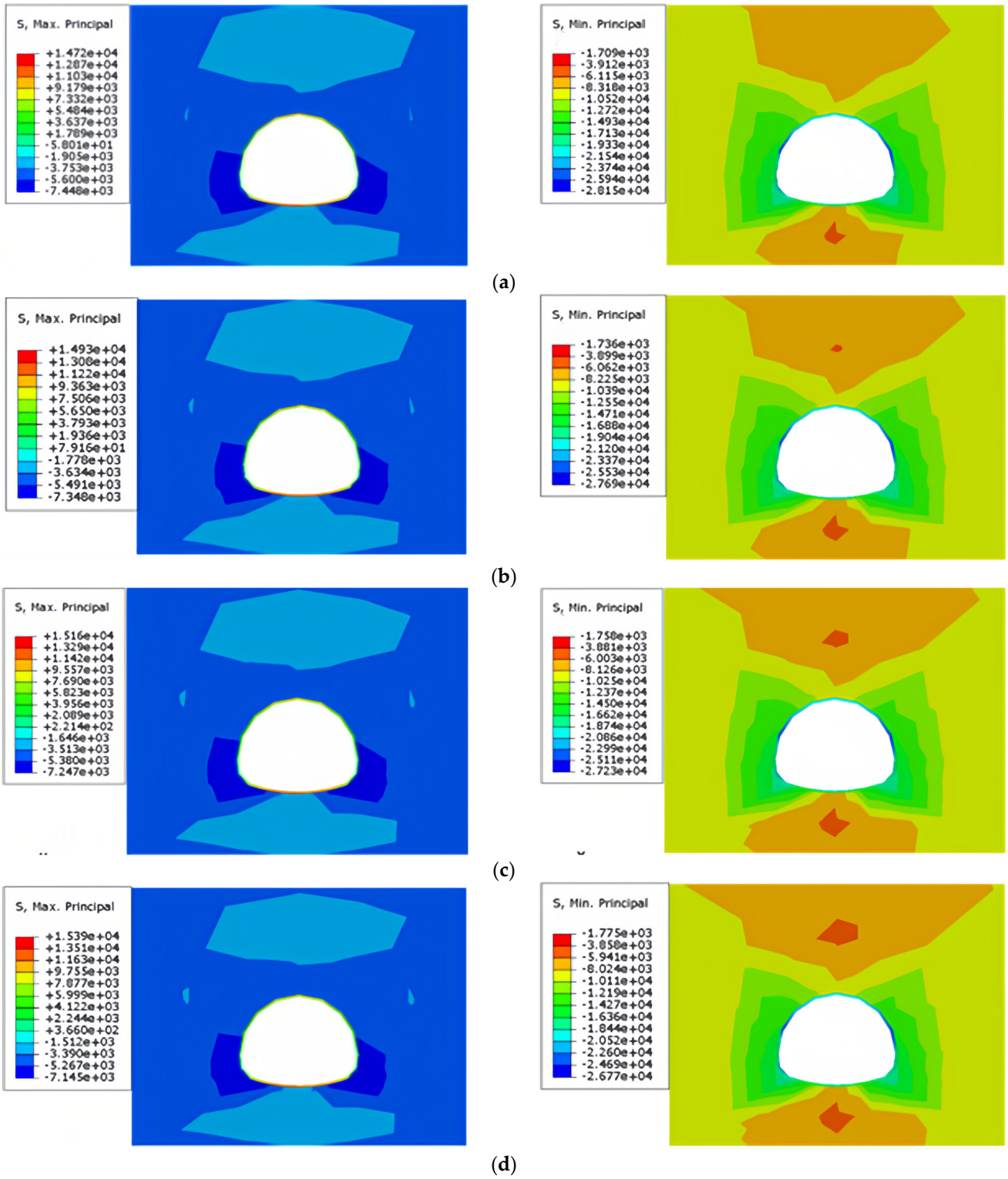

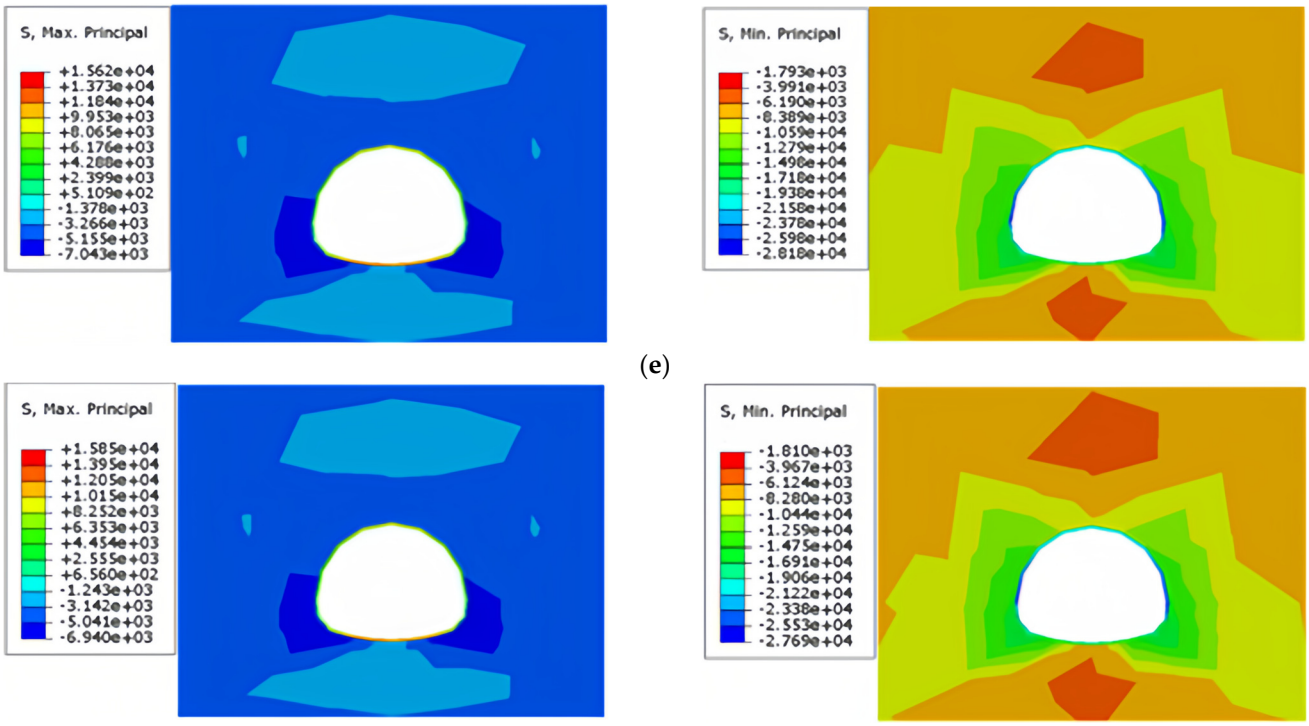

Figure 13. Maximum and minimum stress contour maps under different initial head heights using the FFEM. (In the figure, (**a**): H = 122 m; (**b**): H = 162 m; (**c**): H = 202 m; (**d**): H = 242 m; (**e**): H = 282 m; (**f**): H = 322 m.)

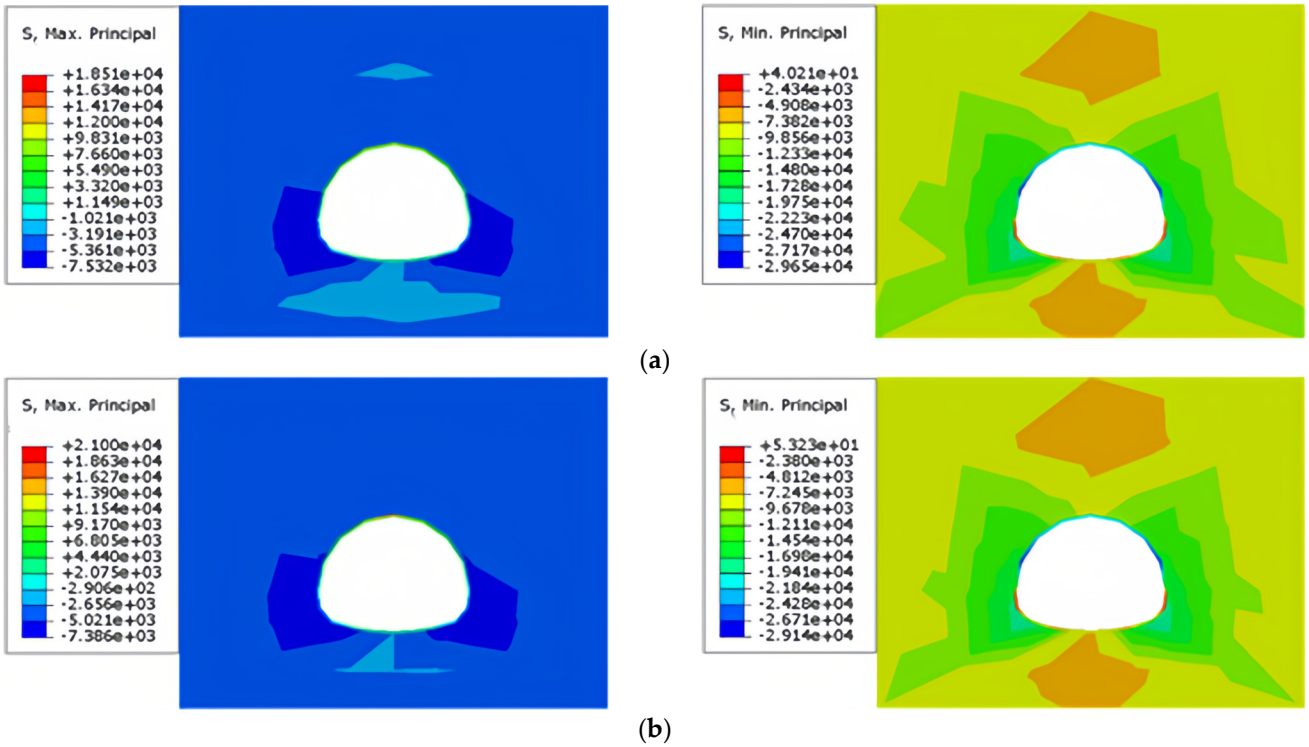

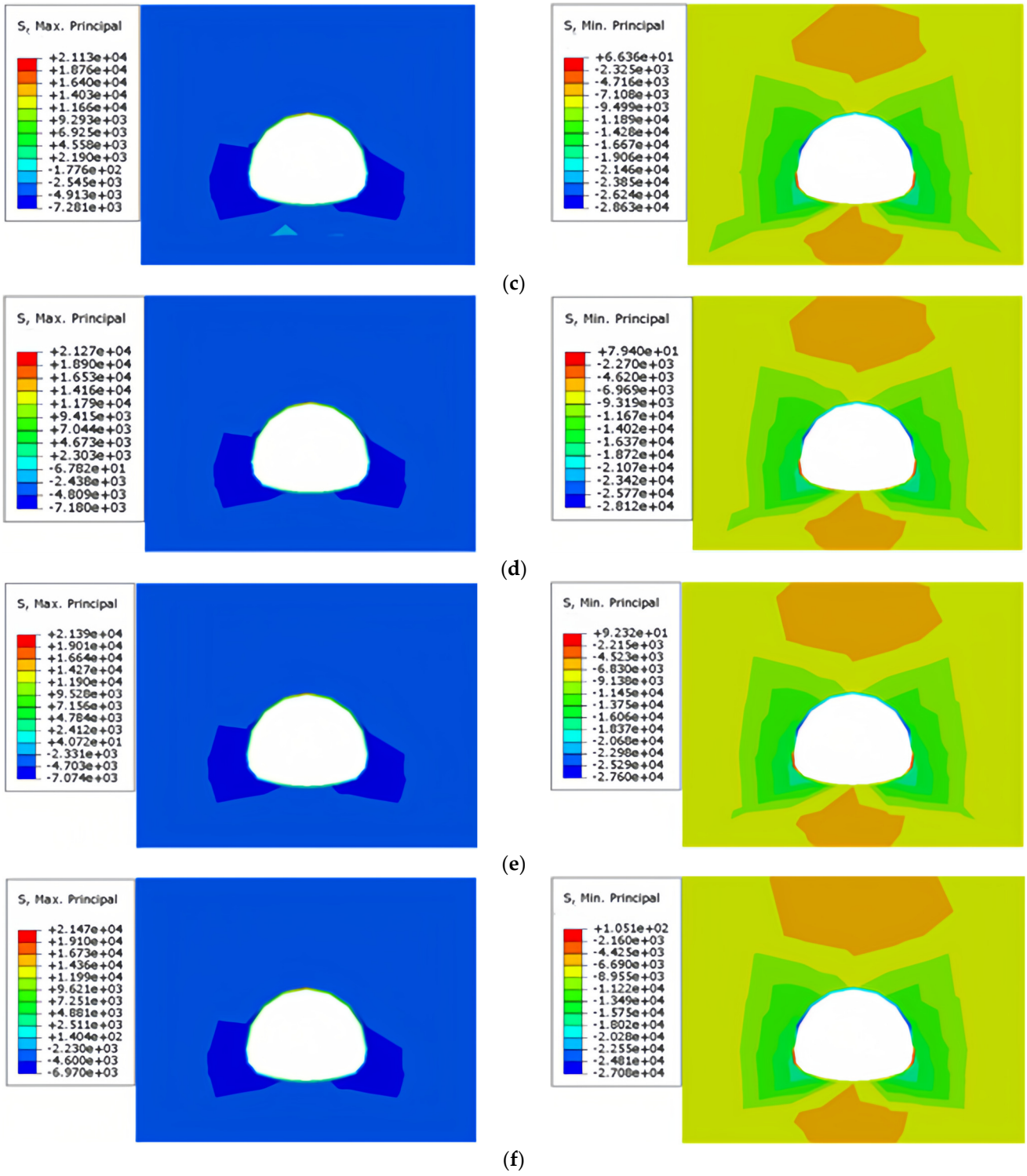

Figure 14. Maximum and minimum stress contour maps under different initial head heights using the BEM. (In the figure, (**a**): H = 122 m; (**b**): H = 162 m; (**c**): H = 202 m; (**d**): H = 242 m; (**e**): H = 282 m; (**f**): H = 322 m.).

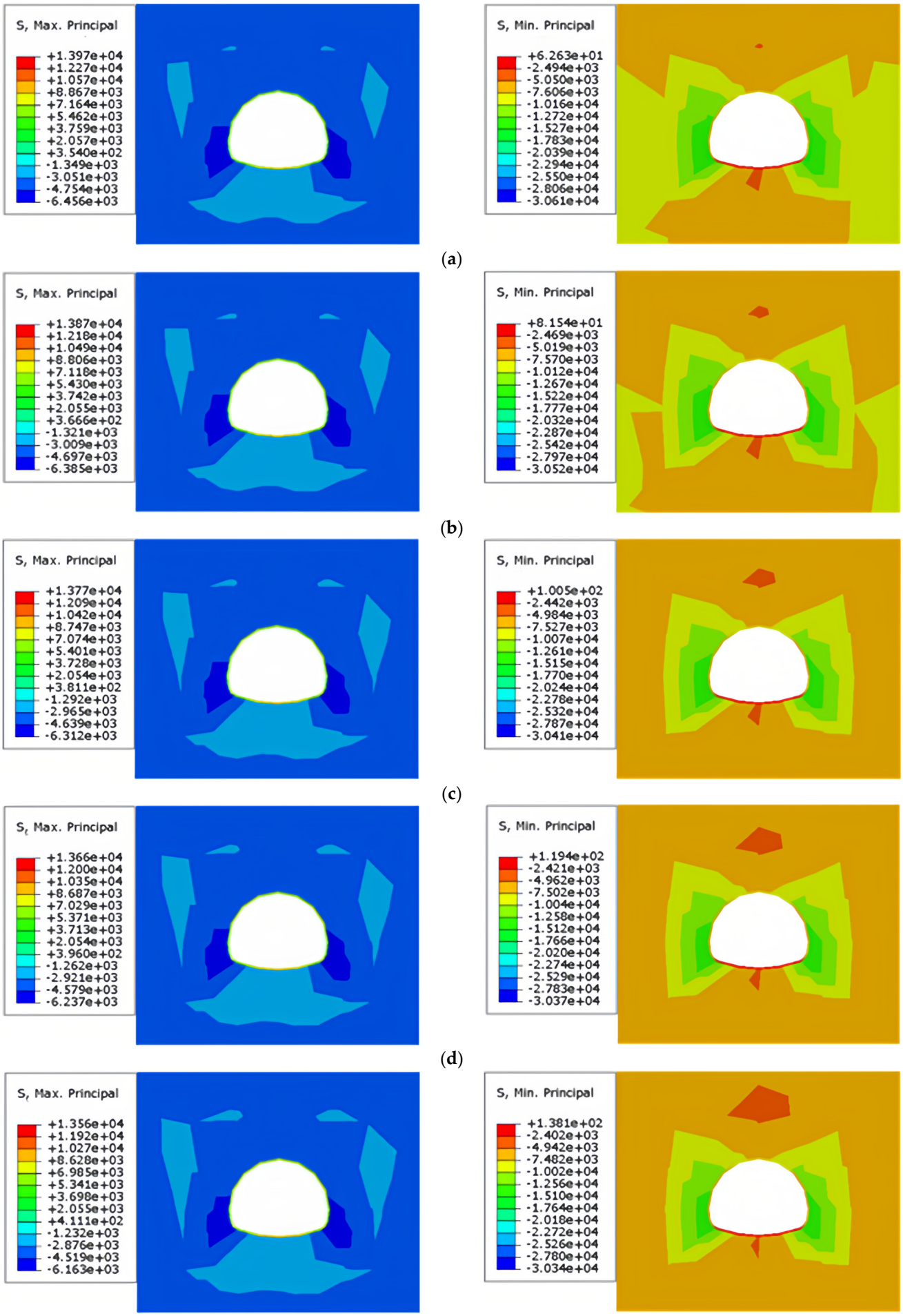
S, Max. Principal
+1.397e+04
+1.227e+04
+1.057e+04
+8.867e+03
+7.164e+03
+5.462e+03
+3.759e+03
+2.057e+03
+3.540e+02
-1.349e+03
-3.051e+03
-4.754e+03
-6.456e+03
S, Min. Principal
+6.263e+01
-2.494e+03
-5.050e+03
-7.606e+03
-1.016e+04
-1.272e+04
-1.527e+04
-1.783e+04
-2.039e+04
-2.294e+04
-2.550e+04
-2.806e+04
-3.061e+04
(a)
S, Max. Principal
+1.387e+04
+1.218e+04
+1.049e+04
+8.806e+03
+7.118e+03
+5.430e+03
+3.742e+03
+2.055e+03
+3.666e+02
-1.321e+03
-3.009e+03
-4.697e+03
-6.385e+03
S, Min. Principal
+8.154e+01
-2.469e+03
-5.019e+03
-7.570e+03
-1.012e+04
-1.267e+04
-1.522e+04
-1.777e+04
-2.032e+04
-2.287e+04
-2.542e+04
-2.797e+04
-3.052e+04
(b)
S, Max. Principal
+1.377e+04
+1.209e+04
+1.042e+04
+8.747e+03
+7.074e+03
+5.401e+03
+3.728e+03
+2.054e+03
+3.811e+02
-1.292e+03
-2.965e+03
-4.639e+03
-6.312e+03
S, Min. Principal
+1.005e+02
-2.442e+03
-4.984e+03
-7.527e+03
-1.007e+04
-1.261e+04
-1.515e+04
-1.770e+04
-2.024e+04
-2.278e+04
-2.532e+04
-2.787e+04
-3.041e+04
(c)
S, Max. Principal
+1.366e+04
+1.200e+04
+1.035e+04
+8.687e+03
+7.029e+03
+5.371e+03
+3.713e+03
+2.054e+03
+3.960e+02
-1.262e+03
-2.921e+03
-4.579e+03
-6.237e+03
S, Min. Principal
+1.194e+02
-2.421e+03
-4.962e+03
-7.502e+03
-1.004e+04
-1.258e+04
-1.512e+04
-1.766e+04
-2.020e+04
-2.274e+04
-2.529e+04
-2.783e+04
-3.037e+04
(d)
S, Max. Principal
+1.356e+04
+1.192e+04
+1.027e+04
+8.628e+03
+6.985e+03
+5.341e+03
+3.698e+03
+2.055e+03
+4.111e+02
-1.232e+03
-2.876e+03
-4.519e+03
-6.163e+03
S, Min. Principal
+1.381e+02
-2.402e+03
-4.942e+03
-7.482e+03
-1.002e+04
-1.256e+04
-1.510e+04
-1.764e+04
-2.018e+04
-2.272e+04
-2.526e+04
-2.780e+04
-3.034e+04

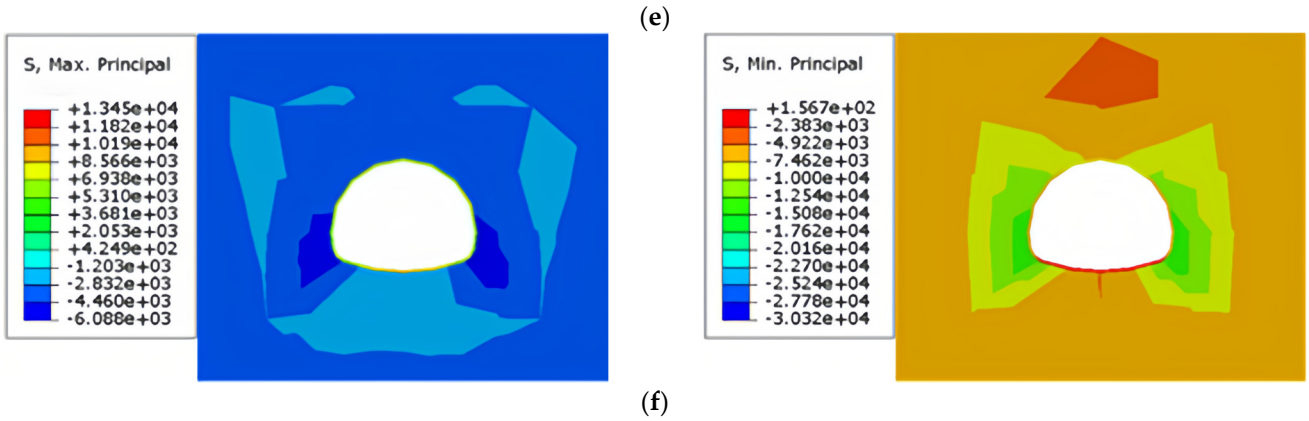

Figure 15. Maximum and minimum stress contour maps under different initial water head heights using the RCSEM. (In the figure, (**a**): H = 122 m; (**b**): H = 162 m; (**c**): H = 202 m; (**d**): H = 242 m; (**e**): H = 282 m; (**f**): H = 322 m.).

To better visualize the stress variation at the monitoring points, the ratio of the principal stress under different working conditions to the principal stress under the initial working condition is defined as the variation rate Δ′. The specific formula is as follows:

$$\Delta' = \frac{\sigma}{\sigma_0} \times 100\% \quad (6)$$

where Δ′ is stress variation rate; σ is principal stress at the monitoring point under different working conditions; σ_0 is principal stress at the monitoring point under the initial working condition.

In the analysis with different initial water head heights, H = 122 m is used as the initial working condition. In the analysis with different excavation methods, the principal stress at each measurement point under the FFEM is used as the initial working condition. The rock mass principal stress variation curve is shown in Figure 16, and the variation rate curve is shown in Figure 17.

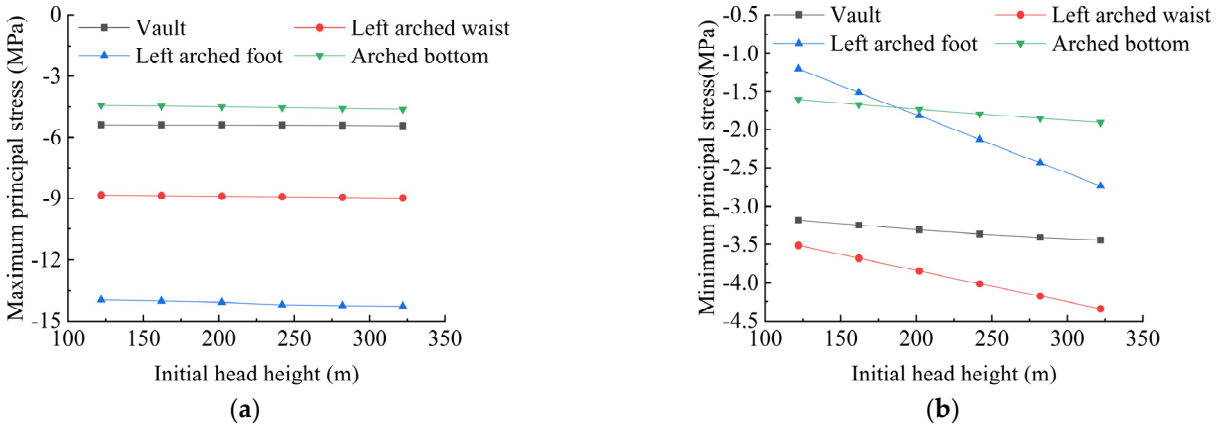

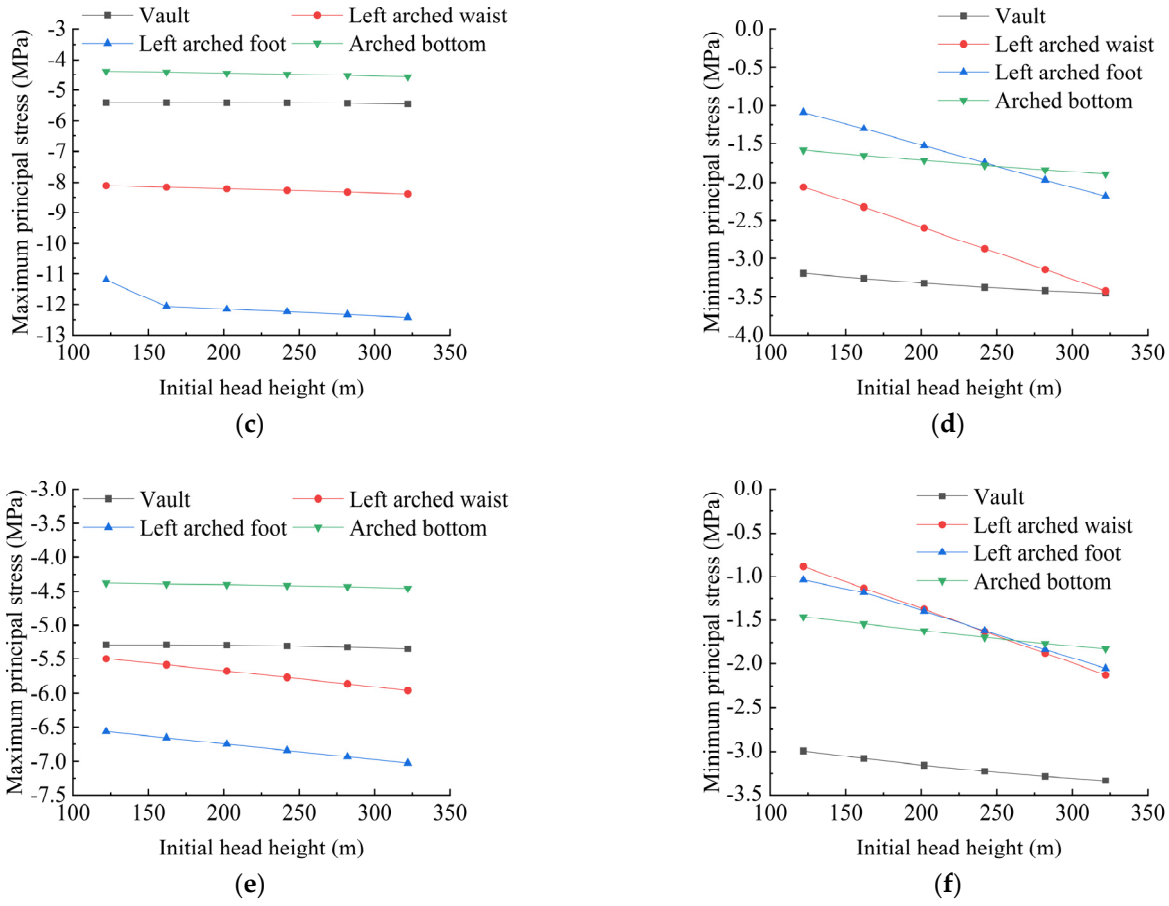

Figure 16. Principal stress at each measurement point for different initial head heights. (In the figure, (**a**): Maximum principal stress at each measurement point under the FFEM; (**b**): Minimum principal stress at each measurement point under the FFEM; (**c**): Maximum principal stress at each measurement point under the BEM; (**d**): Minimum principal stress at each measurement point under the BEM; (**e**): H = Maximum principal stress at each measurement point for the RCSEM; (**f**): Minimum principal stress at each measurement point for the RCSEM.).

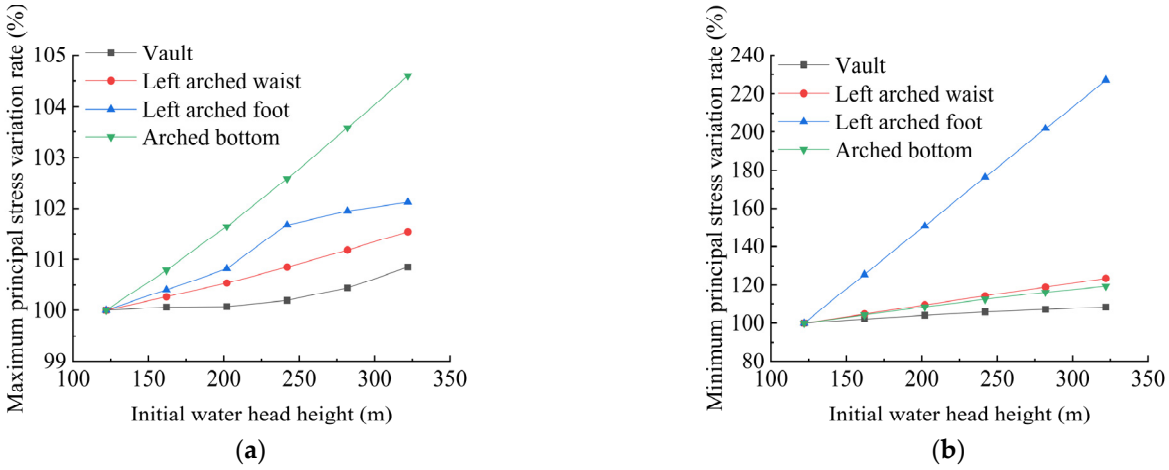

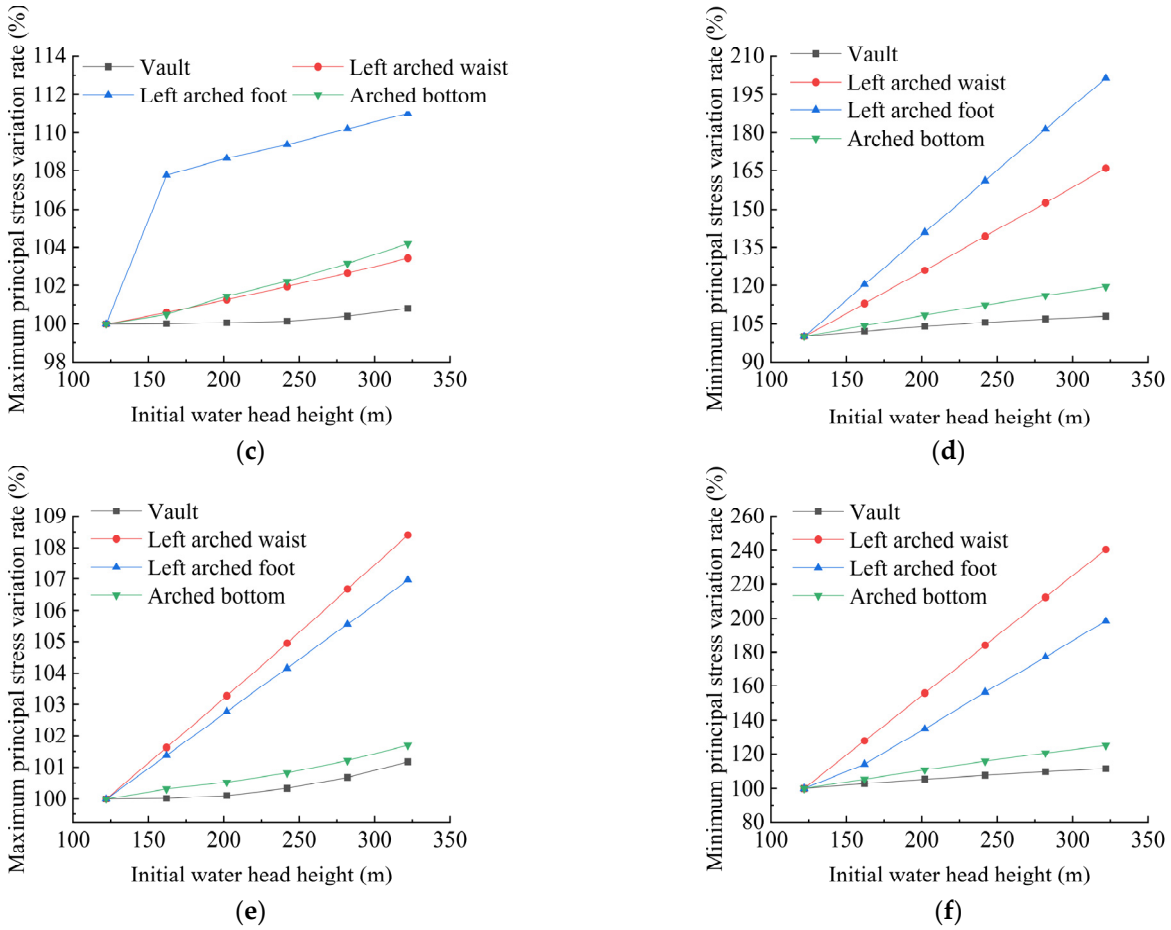

Figure 17. Principal stress variation rate at each measurement point for different initial water head heights. (In the figure, (**a**): Maximum principal stress variation rate at each measurement point for the FFEM; (**b**): Minimum principal stress variation rate at each measurement point for the FFEM; (**c**): Maximum principal stress variation rate at each measurement point for the BEM; (**d**): Minimum principal stress variation rate at each measurement point for the BEM; (**e**): Maximum principal stress variation rate at each measurement point for the RCSEM; (**f**): Minimum principal stress variation rate at each measurement point for the RCSEM.)

(1) As shown in the figures, the maximum and minimum principal stresses at all monitoring points around the tunnel increase gradually with the increase in the initial water level. Under different excavation methods, the monitoring points at all conditions are in a compressive state, and the principal compressive stress has not exceeded 15.33 MPa.

(2) With the increase in the initial water head height, the maximum principal stress at the arch waist left arch waist, and arch bottom increases slightly. The maximum principal stress is compressive, with a relatively low baseline. However, the maximum principal stress at the arch foot is significantly higher than at other monitoring points for all three excavation methods, indicating that the arch foot is a sensitive area for groundwater, posing a certain risk to the stability of the tunnel surrounding rock. It is necessary to apply initial support in time during construction to restrict the increase in surrounding rock stress. Additionally, the maximum principal stress at the arch foot in the RCSEM is much lower than that in the FFEM and BEMs, indicating that the RCSEM is preferred for this project.

(3) As the initial water head height increases, the minimum principal stress at the arch waist and arch foot increases significantly. Since the minimum principal stress is compressive and has a relatively low baseline, even though the minimum principal

stress at the arch waist and arch foot increases substantially under high water levels, its impact on the stability of the tunnel surrounding rock is not significant. Moreover, the minimum principal stress vaults at all monitoring points in the RCSEM are lower than those in the FFEM and BEMs, suggesting that the RCSEM is more suitable for the tunnel excavation in this project.

3.3.2. Displacement Field Analysis Under Different Initial Water Head Heights

Rock mass displacement, as a direct indicator of tunnel stability, undergoes significant changes under the combined effects of excavation disturbances and seepage fields. This section analyzes the excavation displacement fields of the FFEM, BEM, and RCSEM, considering fluid–solid coupling effects. Figures 18–20 show the displacement field contour maps for the different excavation methods.

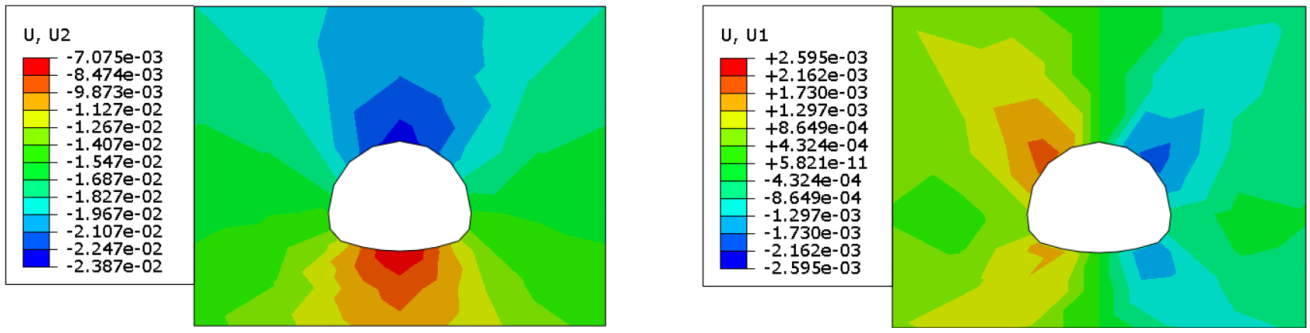

(**a**)

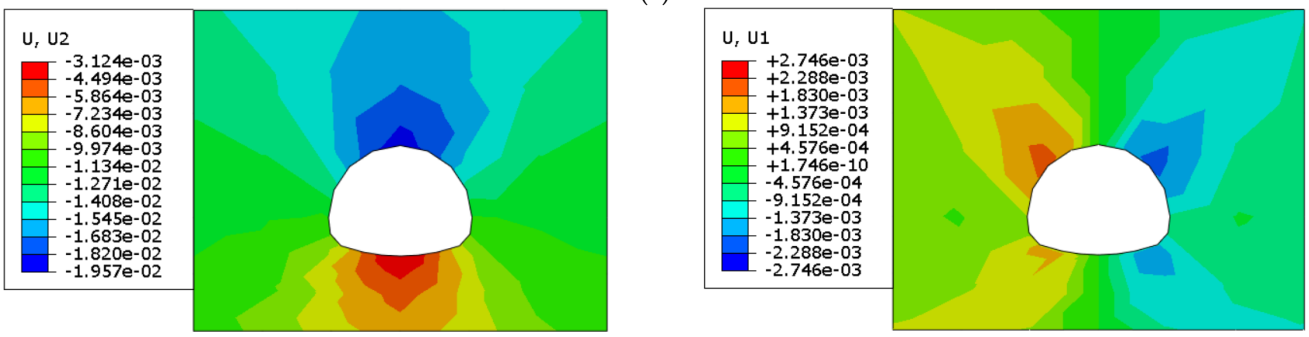

(**b**)

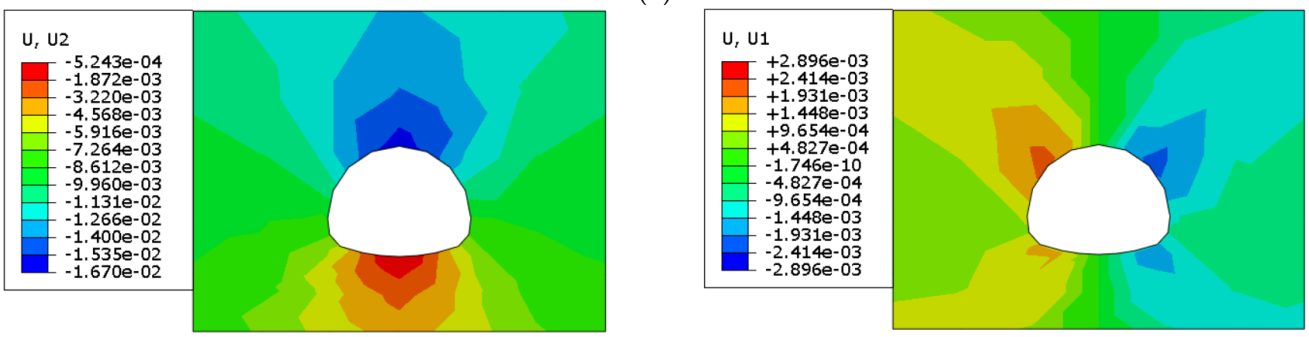

(**c**)

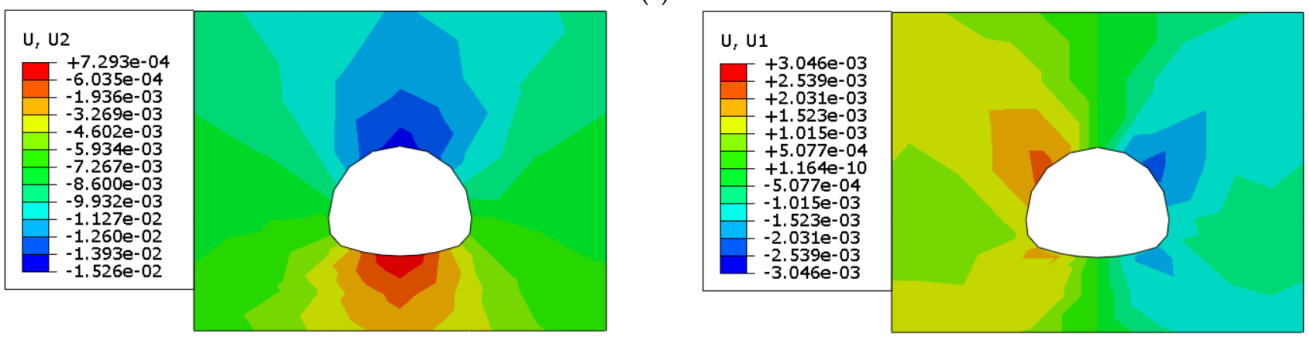

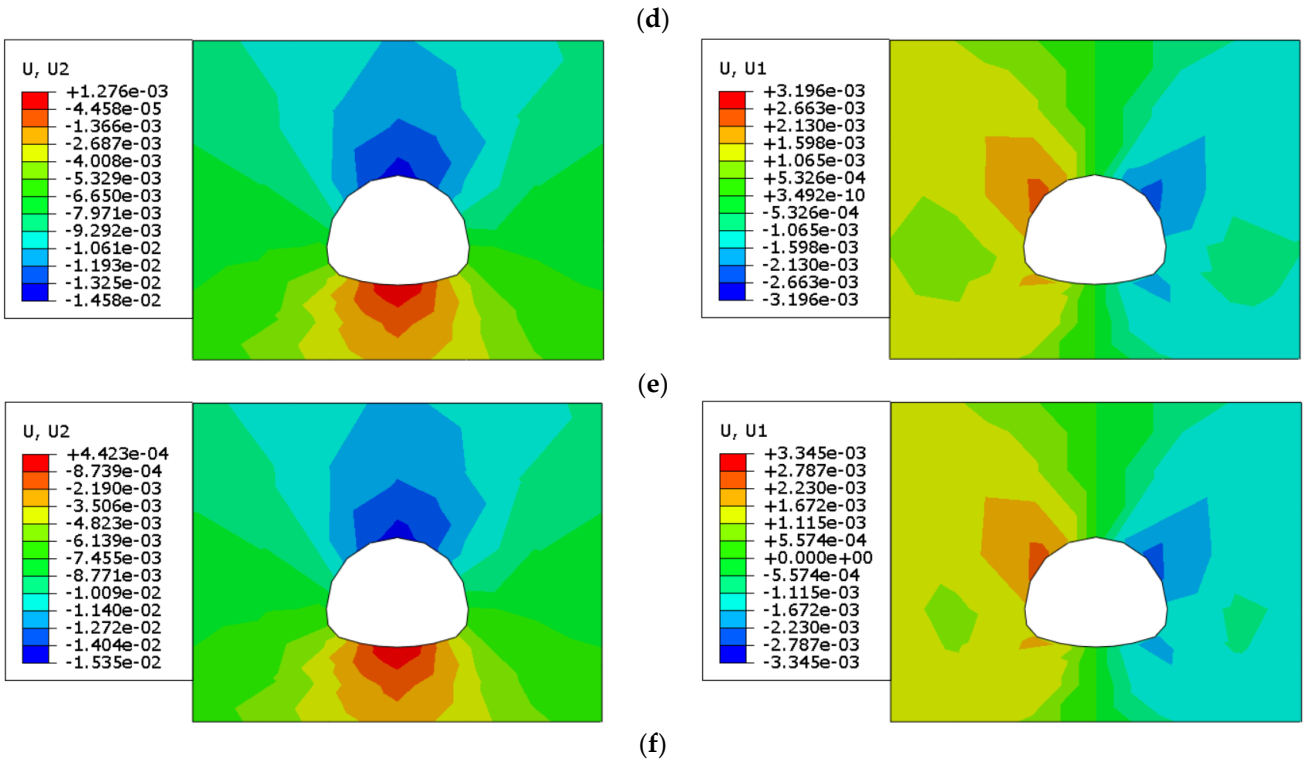

Figure 18. Vertical (U2) and horizontal (U1) displacement contour maps under different initial head heights using the FFEM. (In the figure, (**a**): H = 122 m; (**b**): H = 162 m; (**c**): H = 202 m; (**d**): H = 242 m; (**e**): H = 282 m; (**f**): H = 322 m.).

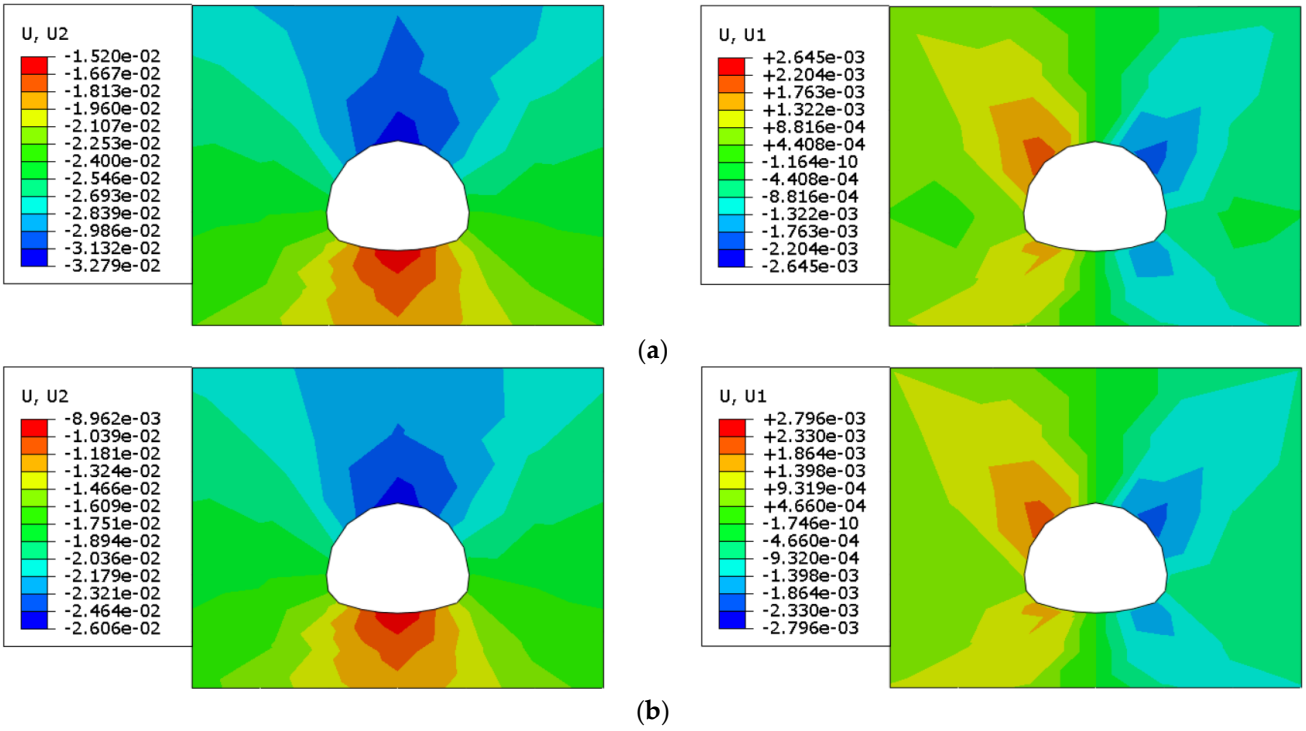

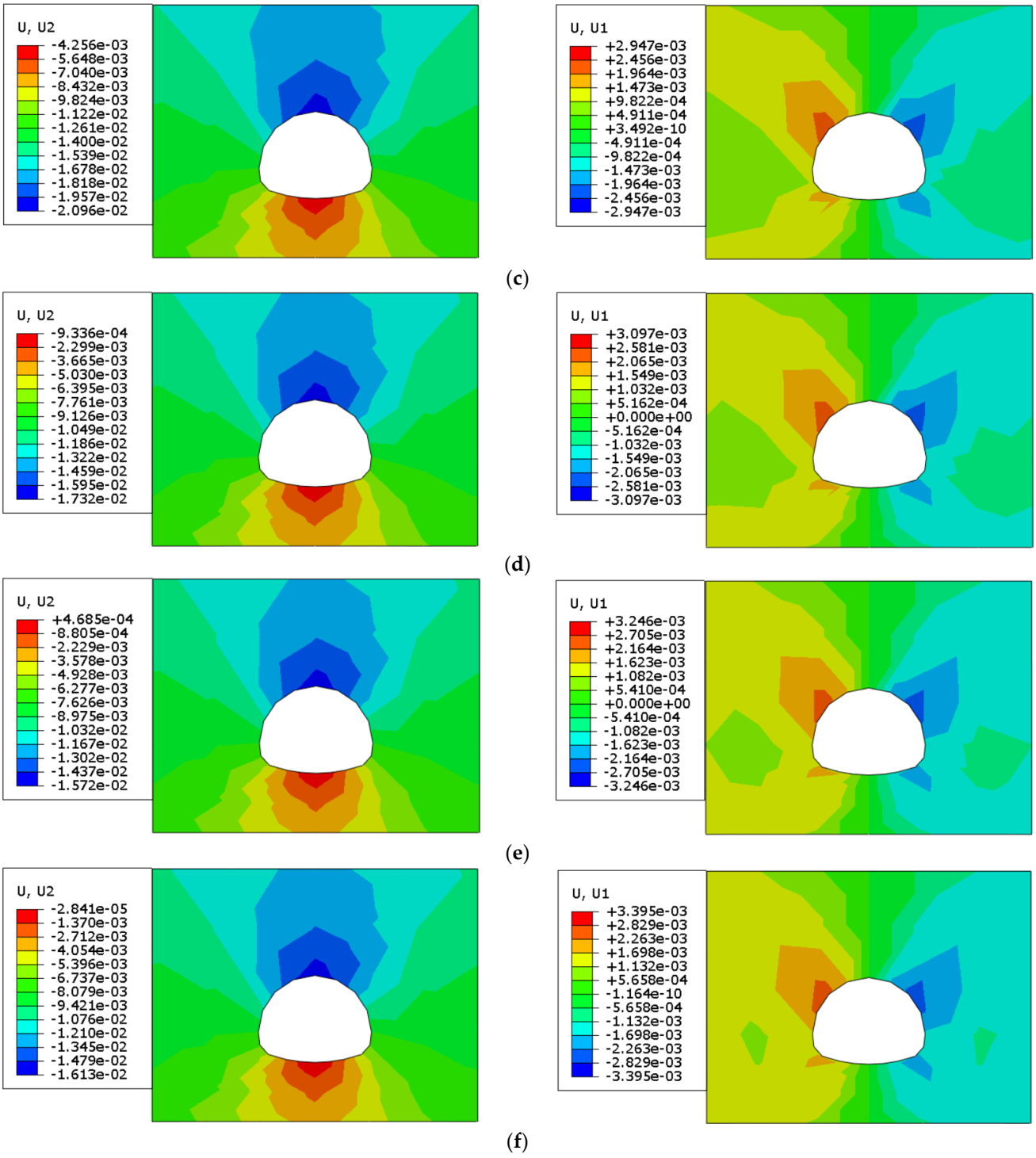

Figure 19. Vertical (U2) and horizontal (U1) displacement contour maps under different initial head heights using the BEM. (In the figure, (**a**): H = 122 m; (**b**): H = 162 m; (**c**): H = 202 m; (**d**): H = 242 m; (**e**): H = 282 m; (**f**): H = 322 m.).

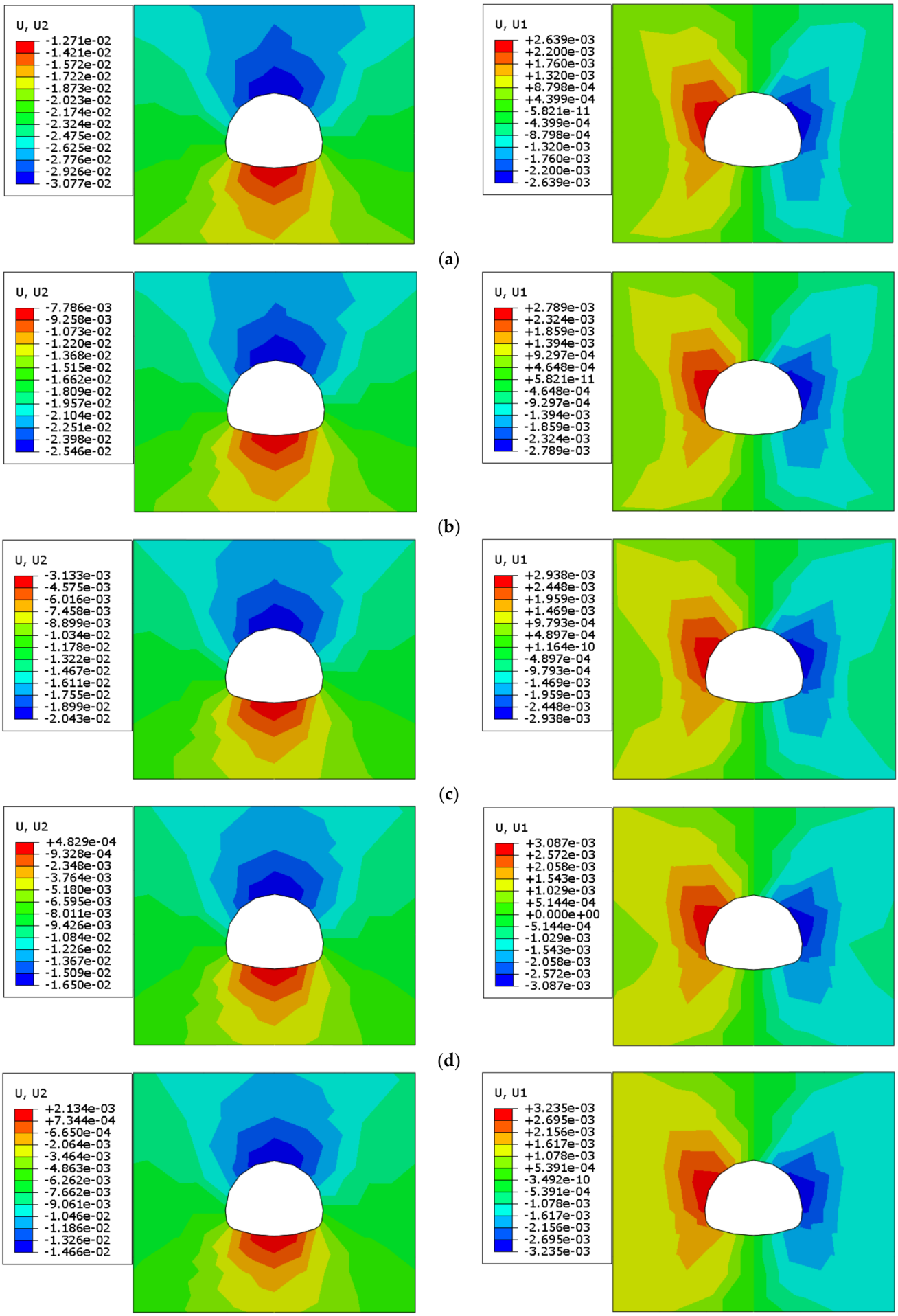
U, U2
-1.271e-02
-1.421e-02
-1.572e-02
-1.722e-02
-1.873e-02
-2.023e-02
-2.174e-02
-2.324e-02
-2.475e-02
-2.625e-02
-2.776e-02
-2.926e-02
-3.077e-02
U, U1
+2.639e-03
+2.200e-03
+1.760e-03
+1.320e-03
+8.798e-04
+4.399e-04
-5.821e-11
-4.399e-04
-8.798e-04
-1.320e-03
-1.760e-03
-2.200e-03
-2.639e-03
(a)
U, U2
-7.786e-03
-9.258e-03
-1.073e-02
-1.220e-02
-1.368e-02
-1.515e-02
-1.662e-02
-1.809e-02
-1.957e-02
-2.104e-02
-2.251e-02
-2.398e-02
-2.546e-02
U, U1
+2.789e-03
+2.324e-03
+1.859e-03
+1.394e-03
+9.297e-04
+4.648e-04
+5.821e-11
-4.648e-04
-9.297e-04
-1.394e-03
-1.859e-03
-2.324e-03
-2.789e-03
(b)
U, U2
-3.133e-03
-4.575e-03
-6.016e-03
-7.458e-03
-8.899e-03
-1.034e-02
-1.178e-02
-1.322e-02
-1.467e-02
-1.611e-02
-1.755e-02
-1.899e-02
-2.043e-02
U, U1
+2.938e-03
+2.448e-03
+1.959e-03
+1.469e-03
+9.793e-04
+4.897e-04
+1.164e-10
-4.897e-04
-9.793e-04
-1.469e-03
-1.959e-03
-2.448e-03
-2.938e-03
(c)
U, U2
+4.829e-04
-9.328e-04
-2.348e-03
-3.764e-03
-5.180e-03
-6.595e-03
-8.011e-03
-9.426e-03
-1.084e-02
-1.226e-02
-1.367e-02
-1.509e-02
-1.650e-02
U, U1
+3.087e-03
+2.572e-03
+2.058e-03
+1.543e-03
+1.029e-03
+5.144e-04
+0.000e+00
-5.144e-04
-1.029e-03
-1.543e-03
-2.058e-03
-2.572e-03
-3.087e-03
(d)
U, U2
+2.134e-03
+7.344e-04
-6.650e-04
-2.064e-03
-3.464e-03
-4.863e-03
-6.262e-03
-7.662e-03
-9.061e-03
-1.046e-02
-1.186e-02
-1.326e-02
-1.466e-02
U, U1
+3.235e-03
+2.695e-03
+2.156e-03
+1.617e-03
+1.078e-03
+5.391e-04
-3.492e-10
-5.391e-04
-1.078e-03
-1.617e-03
-2.156e-03
-2.695e-03
-3.235e-03

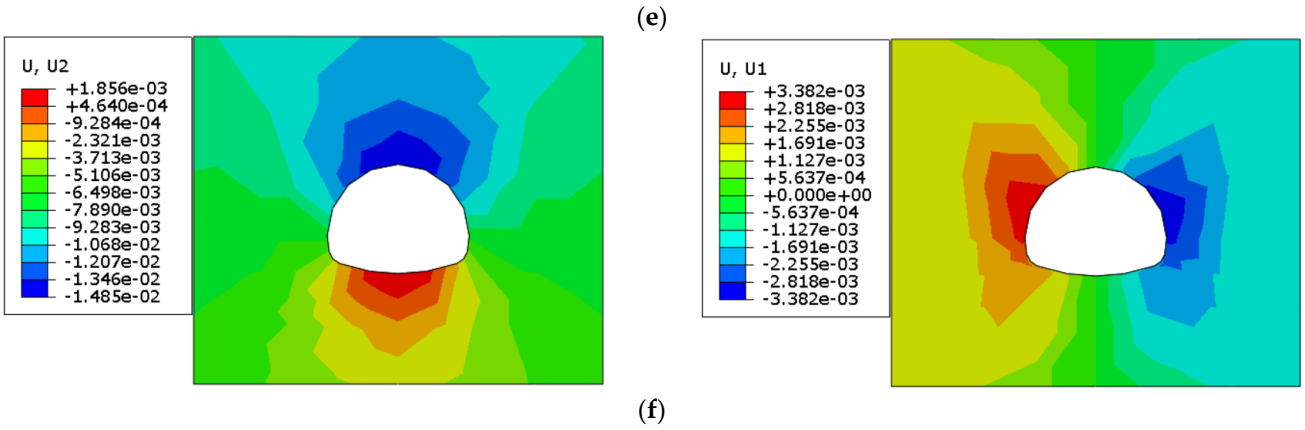

Figure 20. Vertical (U2) and horizontal (U1) displacement contour maps under different initial head heights using the RCSEM. (In the figure, (**a**): H = 122 m; (**b**): H = 162 m; (**c**): H = 202 m; (**d**): H = 242 m; (**e**): H = 282 m; (**f**): H = 322 m.).

To more intuitively describe the variation pattern of surrounding rock displacement, the displacement ratio between monitoring points under different conditions and the initial condition is defined as the change rate Δ. The specific formula is as follows:

$$\Delta' = \frac{u}{u_0} \times 100\% \tag{7}$$

where Δ is displacement variation rate; u is displacement at monitoring points under different conditions (mm); u_0 is displacement at monitoring points under initial conditions (mm).

In the analysis of the same excavation method under different initial water head heights, an initial water head height of 122 m is used as the reference condition, while other water head heights are considered as different working conditions. The displacement variation curves are shown in Figure 21, and the displacement variation rate curves for different excavation methods are shown in Figure 22.

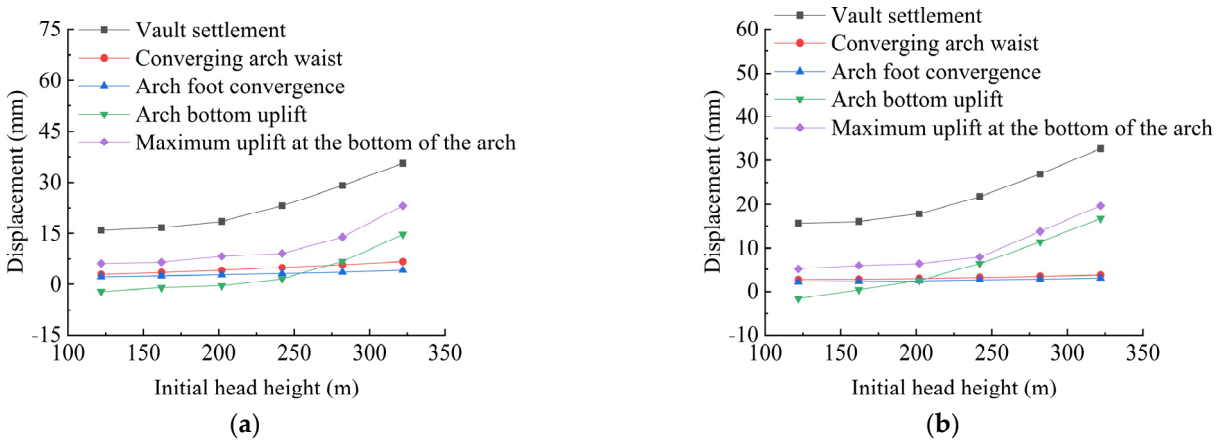

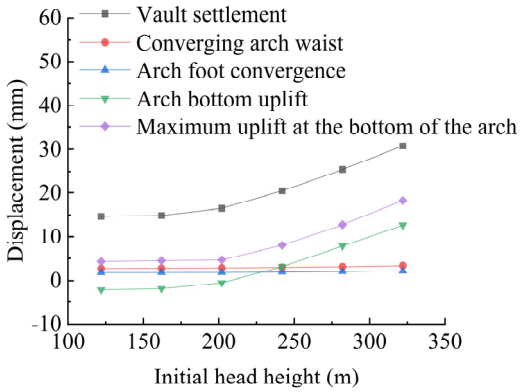

(**c**)

Figure 21. The displacement with the different initial head heights. (In the figure, (**a**): FFEM; (**b**): BEM; (**c**): RCSEM.).

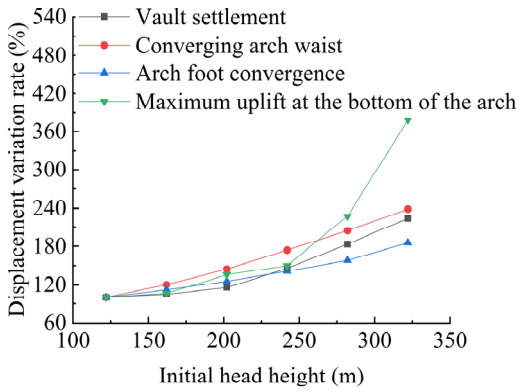

(**a**)

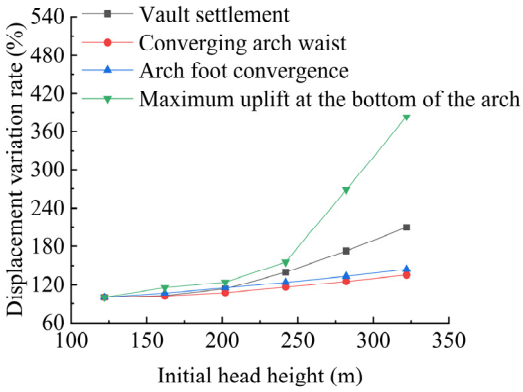

(**b**)

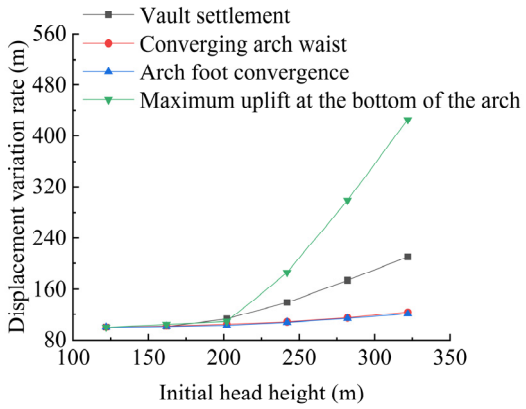

(**c**)

Figure 22. The displacement variation rate with the different initial head heights. (In the figure, (**a**): FFEM; (**b**): BEM; (**c**): RCSEM.).

(1) From the displacement curves of different monitoring points for various excavation methods, it can be seen that their vaults have not exceeded the horizontal convergence limit of the surrounding rock (129.8 mm) and the arch waist settlement limit (64.9 mm). The vault displacement increases significantly with the rise in initial water head height. The convergence vaults at the arch waist and arch foot are less affected by changes in the initial water level compared to the vault and bottom.

(2) The sensitivity of different excavation methods to initial head height is ranked as follows: for the FFEM, the sensitivity is: arch bottom uplift > left arch waist convergence > arch waist settlement > arch foot convergence; for the BEM, the sensitivity is: arch bottom uplift > arch waist settlement > arch foot convergence > left arch waist convergence; for the RCSEM, the sensitivity is: arch bottom uplift > arch waist settlement > left arch waist convergence > arch foot convergence. It is clear that all three excavation methods are most sensitive to arch bottom uplift, which is most affected by the groundwater level. Therefore, during the construction of high-pressure water-rich tunnels, it is essential to promptly drain the water from the arch bottom and decide whether to advance the construction of the arch waist arch based on the deformation of the surrounding rock to prevent excessive deformation and potential instability or failure.

3.4. Stability Analysis of Surrounding Rock with Controlled Excavation Progress Using the RCSEM

Based on the conclusions from Sections 3.2 and 3.3, the RCSEM is more suitable for the excavation of the ZK37 + 900 to ZK38 + 100 section of the Wufu Tunnel. However, for this section, with an average water head of 242 m, the minimum principal stress at the left arch waist exceeds the surrounding rock's tensile strength vault of 1.4 MPa. Therefore, the excavation progress will be controlled to ensure the stability of the surrounding rock. The size of the excavation progress has a significant impact on surrounding rock stability. The larger the excavation progress, the greater the proportion of displacement released from the current excavation clearance in the total displacement, leading to a larger final deformation of the surrounding rock. Conversely, smaller excavation progress results in less disturbance to the surrounding rock and greater stability improvement. This section defines the excavation progress as L and takes five different vaults: L = 0.5 m, L = 1.0 m, L = 1.5 m, L = 2.0 m, and L =2.5 m. The stress and displacement field changes in the surrounding rock for the RCSEM are simulated under these five conditions to determine appropriate excavation progress for guiding the construction.

3.4.1. Stress Field Analysis at Different Excavation Progresses

Tunnel excavation causes a redistribution of the surrounding rock stress. Controlling the excavation footage can reduce the degree of stress concentration, promote a more uniform redistribution of stress, and reduce surrounding rock failure and tunnel structural damage caused by stress concentration. This section analyzes the surrounding rock stress field under different excavation progress for the RCSEM. Figure 23 shows the maximum and minimum principal stress contour plots of the surrounding rock in the monitoring section.

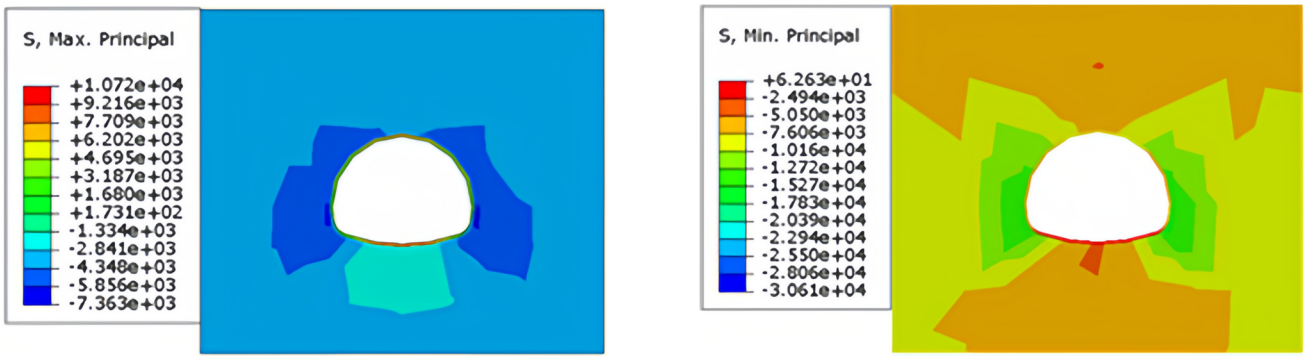

(**a**)

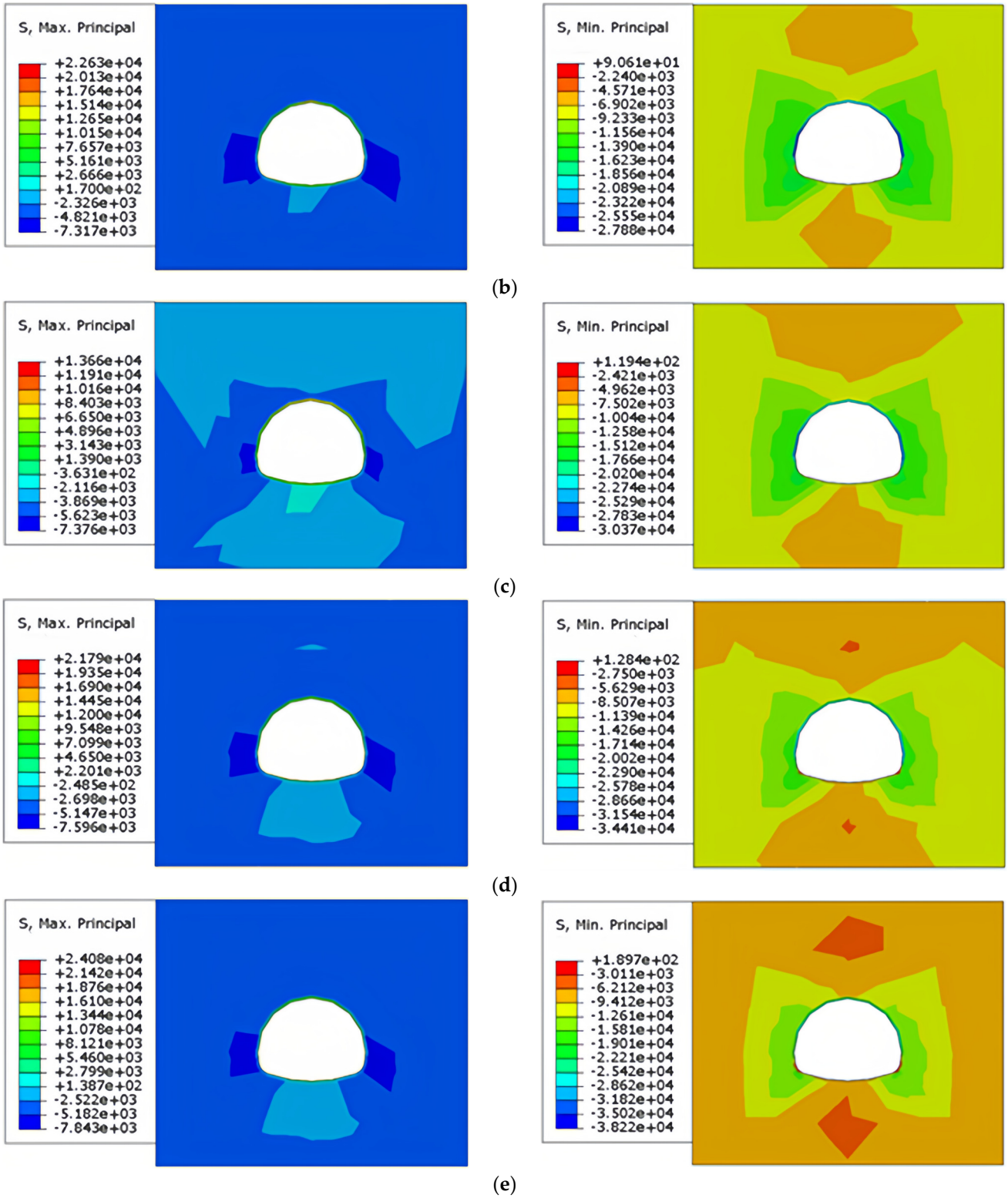

Figure 23. Maximum and minimum stress contour maps under different excavation progress using the RCSEM. (In the figure, (**a**): L = 0.5 m; (**b**): L = 1.0 m; (**c**): L =1.5 m; (**d**): L = 2.0 m; (**e**): L = 2.5 m.)

In the analysis of different initial water head heights, the excavation progress of L = 0.5 m is taken as the initial condition. In the analysis of different excavation methods, the main stress at each measurement point under the FFEM is used as the initial condition. The main stress variation curve of the surrounding rock is shown in Figure 24, and the variation rate curve is shown in Figure 25.

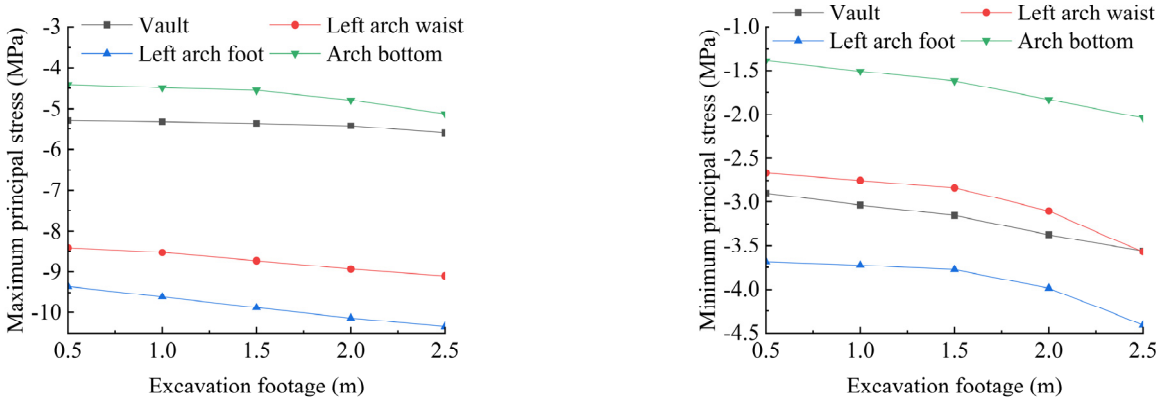

(**a**) (**b**)

Figure 24. Principal stresses at each measurement point for the RCSEM under different excavation footages. (In the figure, (**a**): Maximum principal stress at each measurement point; (**b**): Minimum principal stress at each measurement point.)

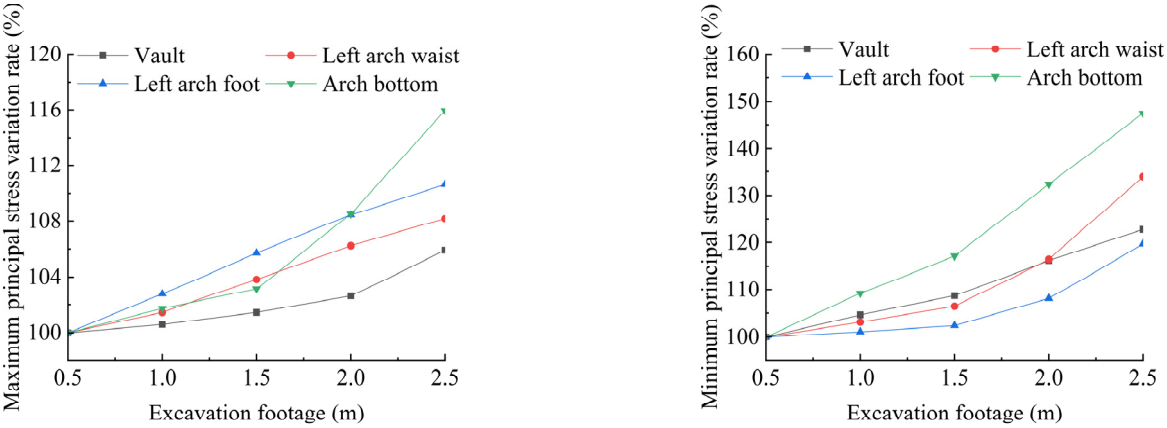

(**a**) Maximum principal stress variation rate at each measurement point (**b**) Minimum principal stress variation rate at each measurement point

Figure 25. Variation rate of principal stress at each measurement point under different excavation footages using the RCSEM. (In the figure, (**a**): Maximum principal stress variation rate at each measurement point; (**b**): Minimum principal stress variation rate at each measurement point.)

(1) According to the figures, the maximum and minimum principal stresses at the monitoring points of the surrounding rock increase gradually with the increase in excavation footage. All monitoring points are in a compressive state, with the principal compressive stress not exceeding 15.33 MPa. As the excavation footage increases, the maximum and minimum principal stresses at each monitoring point also increase. The magnitude of the increase in maximum principal stress at the monitoring points follows the order: invert > left arch foot > left arch waist > arch waist. For the minimum principal stress, the magnitude of increase follows the order: invert > left arch waist > arch waist > left arch foot.

(2) Considering the stability of the surrounding rock and construction safety, it is recommended to adopt the RCSEM with excavation footage of L = 0.5 m for construction in complex geological conditions with high water pressure and karst geology, ensuring the safety and stability of the surrounding rock.

3.4.2. Displacement Field Analysis Under Different Excavation Footages

Reducing the excavation footage can slow down the deformation rate of the surrounding rock, allowing construction personnel to promptly install support measures,

thereby effectively controlling rock displacement. Smaller excavation footages helps reduce the peak deformation of the surrounding rock, minimizing instability and displacement in the ground around the tunnel. This section analyzes the displacement field of surrounding rock under different excavation footages using the RCSEM. Figure 26 shows the vertical and horizontal displacement contour maps of the monitored cross-section.

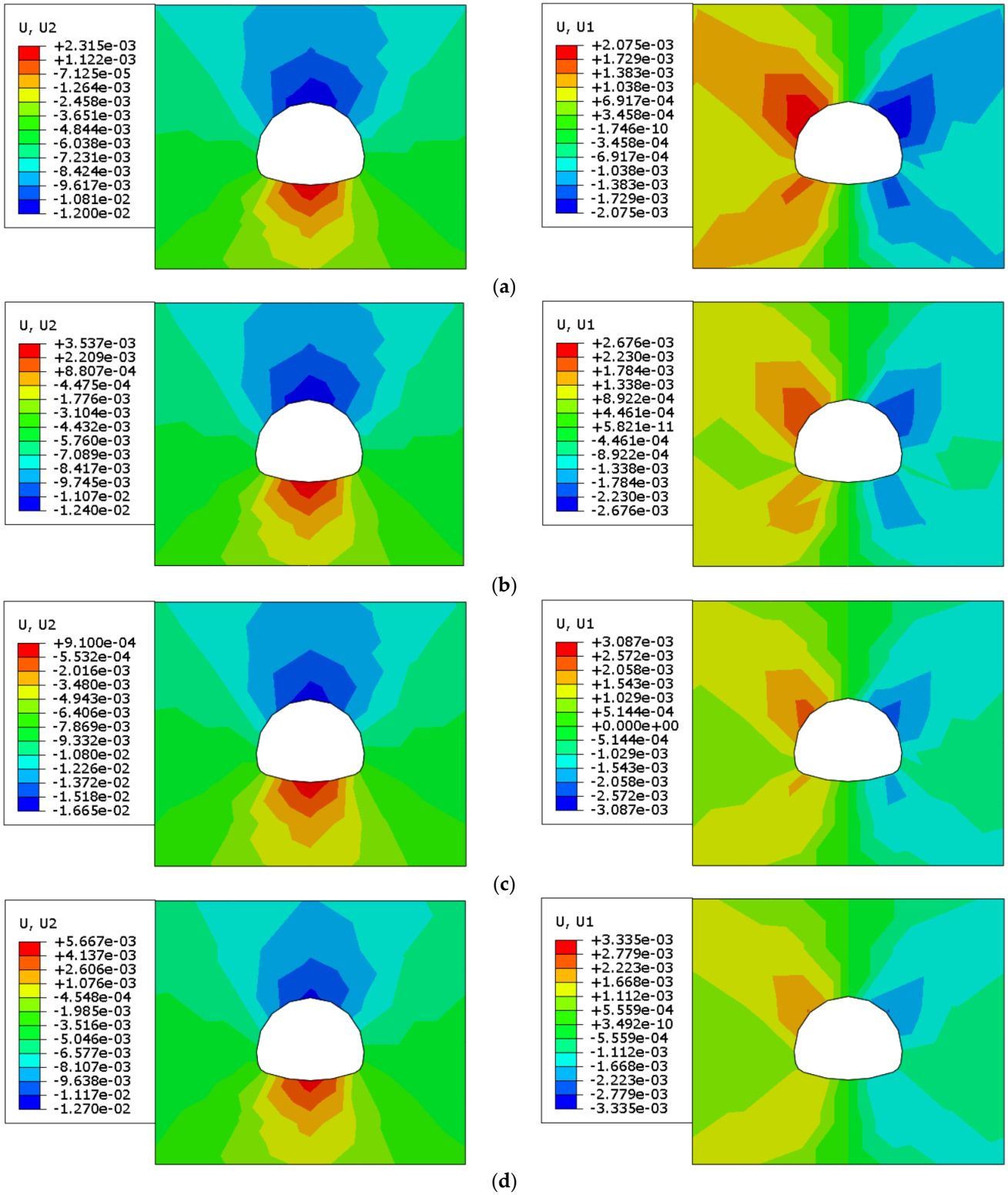

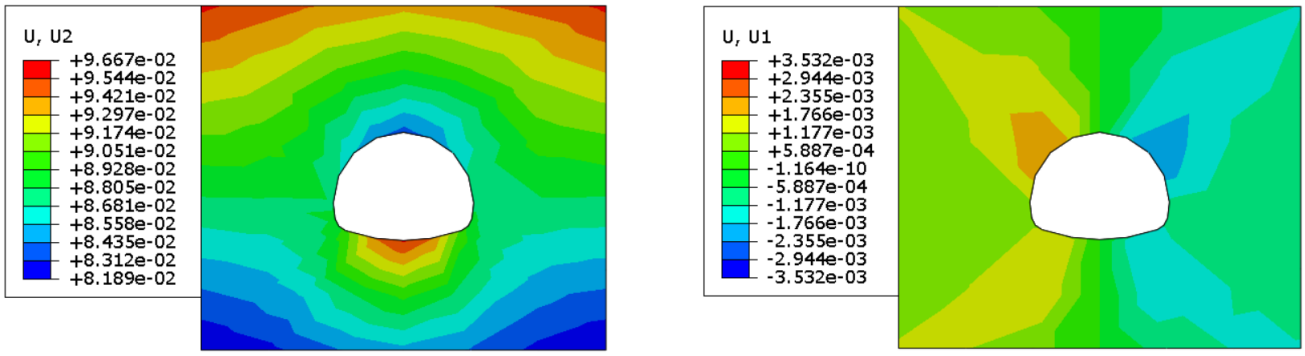

(**e**)

Figure 26. Vertical (U2) and horizontal (U1) displacement contour maps under different excavation footages using the RCSEM. (In the figure, (**a**): L = 0.5 m; (**b**): L = 1.0 m; (**c**): L =1.5 m; (**d**): L = 2.0 m; (**e**): L = 2.5 m.)

In the analysis of different initial water head heights, the excavation footage of L = 0.5 m is used as the initial condition. In the analysis of different excavation methods, the displacement of each monitoring point under different conditions is used as the initial condition. The curves of rock mass displacement variation and variation rate are shown in Figure 27.

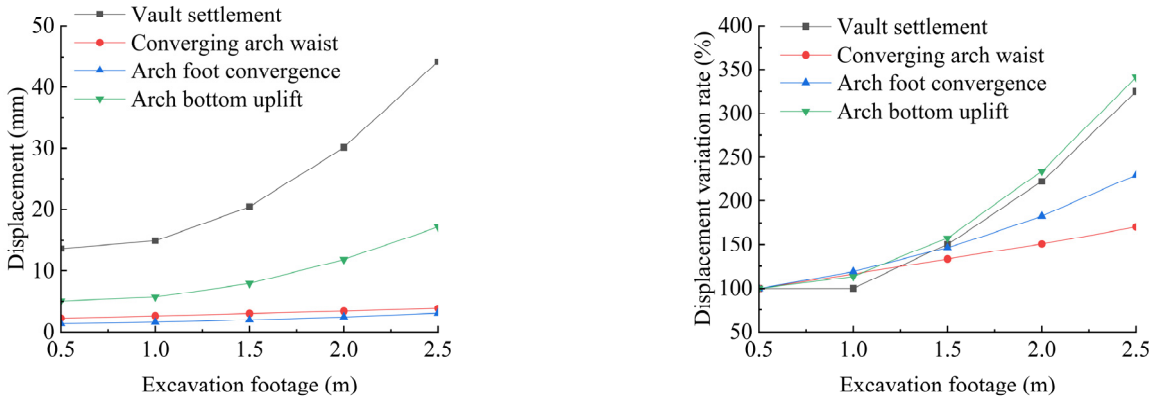

(**a**) (**b**)

Figure 27. Displacement variation patterns at each monitoring point for different excavation footage using the RCSEM. (In the figure, (**a**): Displacement variation curves for each monitoring point; (**b**): Displacement variation rate for each monitoring point.)

(1) From the displacement curves at each monitoring point, it can be seen that the maximum vaults do not exceed the limit vaults of the surrounding rock horizontal convergence (129.8 mm) and the arch waist settlement (64.9 mm). The displacement vaults at the monitoring points are ranked as follows: arch waist settlement > arch bottom uplift > left arch waist convergence > arch foot convergence.

(2) It can be observed that the sensitivity of the RCSEM excavation to the increase in excavation footage is in the following order: arch bottom uplift > arch waist settlement > arch foot convergence > left arch waist convergence. This indicates that controlling the excavation footage can effectively reduce the displacement at each monitoring point. Specifically, for the arch waist settlement and arch bottom uplift, which have larger displacement bases, using a smaller excavation footage can effectively improve the stability and safety of the surrounding rock during the RCSEM.

4. Conclusions

Based on the engineering and geotechnical data, the flow–solid coupling numerical simulation was conducted using ABAQUS 2022 software to analyze the changes in the stress field, displacement field, and pore water pressure field during tunnel construction under different excavation methods and initial water head heights:

(1) The study shows that under different excavation methods and initial water head heights, the drainage volume and water level drawdown exhibit significant changes. The contact zone between weakly permeable and highly permeable rock layers is the area with the highest risk of water inrush, where the drainage volume from the tunnel face is the major contributor. The RCSEM is the most effective in reducing the risk. The increase in initial water head height leads to an increase in both water level drawdown and drainage volume. Reducing the excavation footage can reduce groundwater loss to a certain extent. Compared to controlling excavation footage, water level drawdown and drainage volume are more sensitive to increases in initial water head height. The RCSEM results in the smallest drainage volume and water level drawdown and is more sensitive to increases in excavation footage.

(2) Stress field analysis shows that an increase in water head height significantly raises the stress on the surrounding rock, particularly the maximum principal stress at the arch foot, which increases significantly. The RCSEM can effectively control the increase in stress. Displacement field analysis reveals that the uplift displacement at the arch bottom is significantly affected by the groundwater level, especially when the groundwater level is high, with a marked increase in displacement. The RCSEM has a significant effect on controlling the uplift at the arch bottom. Combined with its advantage in controlling groundwater discharge, the RCSEM is superior to the FFEM and the BEM. Considering these factors, the RCSEM is recommended.

(3) Further control of excavation footage with the RCSEM shows that reducing the excavation footage further stabilizes the surrounding rock and improves safety. Considering the actual engineering situation, an excavation footage of 0.5m is recommended. According to the geotechnical report, the average water level of the surrounding rock in this section of the tunnel is 242 m. The corresponding drainage volume and water level drawdown fitting formula for this excavation scheme is shown in Equation (5).

The above three conclusions show that the RCSEM has a positive effect on the FFEM and the BEM in reducing the drainage volume because the reserved core soil method can better reduce the deformation and displacement around the tunnel and better maintain the stability around the tunnel. This will reduce the impact of disturbances in the surrounding rock of the tunnel due to excavation. The drainage volume of the surrounding rock will not change greatly, which reduces the possibility of water inrush in the tunnel, which is an ideal choice for ecological protection. It also demonstrates the potential of RCSEM as a benchmark for sustainable tunneling methods in water-rich areas. The findings provide new ideas for solving similar geological or infrastructural challenges around the world.

Author Contributions: Conceptualization, W.M.; data curation, M.Z. and C.S.; formal analysis, C.S.; funding acquisition, X.Z. (Xiaowei Zhang) and X.L.; investigation, G.T. and J.L., methodology, W.M.; supervision, X.Z. (Xuefu Zhang); writing—original draft, M.Z.; writing—review and editing, M.Z. All authors have read and agreed to the published version of the manuscript.

Funding: This research was funded by the Transportation Technology Program of Chongqing Municipal, grant number (2022-05), the Natural Science Foundation of Chongqing, grant number (2024NSCQ-MSX2527), the Lump-sum System Project of Chongqing Municipal Talent Plan, China,

grant number (cstc2024ycjh-bgzxm0219), and the Cooperation Projects between Universities in Chongqing and Affiliated Institutes of CAS, grant number (HZ2021009).

Data Availability Statement: The original contributions presented in the study are included in the article; further inquiries can be directed to the corresponding author.

Conflicts of Interest: Author Xiaowei Zhang and Xinzhen Li was employed by the company China Railway Changjiang Transport Design Group Co., Ltd. Author Jun Liu was employed by the company Chongqing High Speed Railway Construction Wankaida Expressway Co., Ltd. The remaining authors declare that the research was conducted in the absence of any commercial or financial relationships that could be construed as a potential conflict of interest.

References

1. Li, H.; Kagami, H. Groundwater level and chemistry changes resulting from tunnel construction near Matsumoto City. *Environ. Geol.* **1997**, *31*, 76–84.
2. Sjolander-Lindqvist, A. Conflicting Perspectives on Water in a Swedish Railway Tunnel Project. *Environ. Values*.**2005**, *14*, 221–239.
3. Chae, G.T.; Yun, S.T.; Choi, B.Y.; Yu, S.-Y.; Jo, H.-Y.; Mayer, B.; Kim, Y.-J.; Lee, J.-Y. Hydrochemistry of urban groundwater, Seoul. Korea: The impact of subway tunnels on groundwater quality. *J. Contam. Hydrol.* **2008**, *101*, 42–52.
4. Vincenzi, V.; Gargini, A.; Goldscheider, N. Using tracer tests and hydrological observations to evaluate effects of tunnel drainage on groundwater and surface waters in the Northern Apennines (Italy). *Hydrogeol. J.* **2009**, *17*, 135–150.
5. Raposo, J.R.; Molinero, J.; Dafonte, J. Quantitative evaluation of hydrogeological impact produced by tunnel construction using water balance models. *Eng. Geol.* **2010**, *116*, 323–332.
6. Attanayake, P.M.; Waterman, M.K. Identifying environmental impacts of underground construction. *Hydrogeol. J.* **2006**, *14*, 1160–1170.
7. Arjnoi, P.; Jeong, J.H.; Kim, C.Y.; Park, K.H. Effect of drainage conditions on pore water pressure distributions and lining stresses in drained tunnels. *Tunn. Undergr. Space Technol.* **2009**, *24*, 376–389.
8. Gattinoni, P.; Scesi, L. The groundwater rise in the urban area of Milan (Italy) and its interactions with underground structures and infrastructures. *Tunn. Undergr. Space Technol.* **2017**, *62*, 103–114.
9. Gokdemir, C.; Li, Y.D., Rubin, Y., Li, X.J. Stochastic modeling of groundwater drawdown response induced by tunnel drainage. *Eng. Geol.* **2022**, *297*, 106529.
10. Lv, Y.X.; Jiang, J.; Li, C.; Hu, W.; Jiang, Y. Elaborate simulation and predication of the tunnel drainage effect on karst groundwater field and discharge based on Visual MODFLOW. *J. Hydrol.* **2022**, *612*, 128023.
11. Wu, Y.Q.; Wang, K., Zhang, L.Z.; Peng, S.H. Sand-layer collapse treatment: An engineering example from Qingdao Metro subway tunnel. *J. Clean. Prod.* **2018**, *197*, 19.
12. Xue, Y.G.; Kong, F.M.; Li, S.C.; Qiu, D.; Su, M.; Li, Z.; Zhou, B. Water and mud inrush hazard in underground engineering: Genesis, evolution and prevention. *Tunn. Undergr. Space Technol.* **2021**, *114*, 103987.
13. Zou, Q.L.; Ning, Y.H., Zang, B.C.; Tian, S.; Jiang, Z.; An, Y. Mechanical properties and failure characteristics of sandstone under ramp loading paths. *Geomech. Geophys. Geo-Energy Geo-Resour.* **2023**, *9*, 39.
14. Zou, Q.L.; Chen, Z.H.; Zhan, J.F.; Chen, C.; Gao, S.; Kong, F.; Xia, X. Morphological evolution of fracture channels and flow conduction law after sandstone failure under cyclic loading with different stress levels. *Int. J. Min. Sci. Technol.* **2023**, *33*, 1527–1540.
15. Xue, Y.G.; Li, J.K.; Wang, X.K.; Yang, W.; Qiu, D.; Su, M. Analysis and optimization design of submarine tunnels crossing fault fracture zones based on numerical simulation. *Mar. Georesour. Geotechnol.* **2020**, *38*, 1106–1117.
16. Li, C.C.; Wang, Z.Z.; Liu, Q.H. Numerical Simulation of Mudstone Shield Tunnel Excavation with ABAQUS Seepage-Stress Coupling: A Case Study. *Sustainability* **2023**, *15*, 667.
17. Wang, Y. Coupling characteristics of seepage and stress at a single fracture surface. *Chin. J. Rock Mech. Eng.* **2002**, *9*, 83–87.
18. Huang, T. Study on the coupled effect of seepage-stress-temperature of fractured rock mass. *Chin. J. Rock Mech. Eng.* **2002**, *21*, 77–82.
19. Di, Q.G.; Li, P.F.; Zhang, M.J.; Zhang, W.; Wang, X. Analysis of face stability for tunnels under seepage flow in the saturated ground. *Ocean. Eng.* **2022**, *226*, 112674.
20. Jia, S.P.; Gao, M.; Yu, H.D.; Gong, J. A coupled damage-permeability model of clay stone with high porosity and low permeability and its numerical implementation. *J. Cent. South Univ. (Sci. Technol.)* **2016**, *47*, 558–568.
21. Li, S.C.; Liu, H.L.; Li, L.P.; Zhang, Q.-Q.; Wang, K.; Wang, K. Large scale three-dimensional seepage analysis model test and numerical simulation research on undersea tunnel. *Appl. Ocean. Res.* **2016**, *59*, 510–520.

22. Li, J.L.; Kang, Z.J.; Tan, Y. Parametric Study on Stability of Tunneling Excavation Face via Fluid-Solid Coupling Simulation. In *Tunnelling and Underground Construction, Proceedings of the Geoshanghai 2018 International Conference, Shanghai, China, 27–30 May 2018*; Springer: Cham, Switzerland, 2018; pp. 74–83.
23. Guo, Y.F.; Wang, H.N.; Jiang, M.J. An exact analytical approach for determining the seepage field around underwater twin tunnels with linings. *Transp. Geotech.* **2023**, *42*, 101050.
24. Zhao, J.P.; Li, J.W.; Bi, L.; Cheng, B.B. Analytical solution of seepage field and reasonable support parameters of tunnel in water rich area. *J. Zhejiang Univ. (Eng. Sci.)* **2021**, *55*, 2142–2150.
25. Wang, F.; Li, P.F. An analytical model of seepage field for symmetrical under water tunnels. *Symmetry* **2018**, *10*, 273.
26. Guo, Y.F.; Wang, H.N.; Jiang, M.J. Efficient iterative analytical model for underground seepage around multiple tunnels in semi-infinite saturated media. *J. Eng. Mech.* **2021**, *147*, 04021101.
27. Yu, J.; Zhang, Y.; Li, D.K.; Zheng, J.; Zhang, W. Analytical study of steady state seepage field in tunnels with localized water leakage under the effect of grouting circle. *Tunn. Undergr. Space Technol.* **2024**, *150*, 105854.
28. Zhang, B.Q. Analytical Solution for Seepage Field of Twin-parallel Tunnels in Semi-infinite Plane. *J. China Railw. Soc.* **2017**, *39*, 125–131.
29. Chen, Z.Q.; Li, Z.; He, C.; Ma, C.; Li, X.; Chen, K.; Zhang, H.; Liu, M. Investigation on seepage field distribution and structural safety performance of small interval tunnel in water-rich region. *Tunn. Undergr. Space Technol.* **2023**, *138*, 105172.
30. Wei, F.R.; Wang, H.N.; Zeng, G.S. Analytical Solution to the Seepage Field of Two Parallel Noncircular Tunnels in Permeable Anisotropic Ground. *KSCE J. Civ. Eng.* **2022**, *26*, 5328–5341.
31. Zhang, Z.G.; Wang, J.C.; Zhao, Q.H.; Li, Z.; Zhang, M.; Wu, Z.; Pan, Y. Analytical solution of head distribution on tunnel structure adjacent water-filled fault in water-enriched mountain region. *Chin. J. Rock Mech. Eng.* **2020**, *39*, 3378–3394.
32. Zhu, C.W.; Ying, H.W.; Gong, X.N.; Shen, H.; Wang, X. Analytical solutions to seepage field of underwater twin parallel tunnels. *Chin. J. Geotech. Eng.* **2019**, *41*, 355–360.
33. *JTG 3370.1-2018*; Specifications for Design of Highway Tunnels. China Communications Press: Beijing, China, 2018.
34. *DBJ50-174-2014*; Code for Geological Investigation of Municipal Engineering. Chongqing Municipal Commission of Urban-Rural Development: Chongqing, China, 2014.